THE EXCHANGE OF INORGANIC CARBON ON THE CANADIAN BEAUFORT SHELF

by

Jacoba L. Mol

Submitted in partial fulfillment of the requirements
for the degree of Master of Science

at

Dalhousie University
Halifax, Nova Scotia
April 2017

for Matt

I carry you with me on every adventure.

TABLE OF CONTENTS

LIST OF TABLES

LIST OF FIGURES

ABSTRACT

The Mackenzie Shelf in the southeastern Beaufort Sea is a region that has experienced large changes in the past several decades as warming, sea-ice loss, and increased river discharge have altered carbon cycling. Upwelling and downwelling events are common on the shelf, caused by strong, fluctuating along-shore winds, resulting in cross-shelf Ekman transport. Downwelling carries inorganic carbon and other remineralization products off the shelf and into the deep basin for possible long-term storage in the world oceans. Upwelling carries dissolved inorganic carbon (DIC) and nutrient-rich waters from the Pacific-origin upper halocline layer (UHL) onto the shelf. Profiles of DIC and total alkalinity (TA) taken in August and September of 2014 are used to investigate the cycling of inorganic carbon on the Mackenzie Shelf. The along-shore transport of water and the cross-shelf transport of inorganic carbon is quantified using velocity field output from a simulation of the Arctic and Northern Hemisphere Atlantic (ANHA4) configuration of the Nucleus of European Modelling of the Ocean (NEMO) framework. A strong upwelling event prior to sampling on the Mackenzie Shelf is analyzed and the resulting influence on the carbonate system, including the saturation state of waters with respect to aragonite and pH, is investigated. TA and the oxygen isotope ratio of water ($\delta^{18}O$) are used to examine water mass distributions in the study area and analyze the influence of Pacific Water, Mackenzie River freshwater, and sea-ice melt on carbon dynamics and air-sea fluxes of carbon dioxide (CO_2) in the surface mixed layer. Understanding carbon transfer in this seasonally dynamic environment is key in order to quantify the importance of Arctic shelf regions to the global carbon cycle and to provide a basis for understanding how it will respond to the aforementioned climate-induced changes.

LIST OF ABBREVIATIONS AND SYMBOLS USED

Roman Symbol	Description	Units
ATL	Atlantic water	no units
δ^{13}C-DIC	stable carbon isotopes of DIC	‰
CO_2	Carbon Dioxide	no units
DIC	Dissolved Inorganic Carbon	μmol kg^{-1}
δ^{18}O	stable oxygen isotopes of water	‰
MW	meteoric water	no units
pCO_2	partial pressure of CO_2	μatm
SIM	sea-ice melt	no units
TA	Total Alkalinity	μmol kg^{-1}
UHL	upper halocline layer	no units

Greek Symbol	Description	Units
Ω	calcium carbonate saturation state	no units

ACKNOWLEDGEMENTS

Thank you to my supervisor Helmuth for all the support and guidance along the way. Most of all, thanks for giving me the opportunity to work in the greatest place on earth and never saying no to a cruise. Thanks to my committee members, Markus and Tim, for the support and suggestions.

Thanks to my family, Mom and Dad for always being a phone call, or a car ride, or a plane ride away. I would not have gotten to Pond Inlet without you, or certainty my wallet would not have. Thanks to Lucas for the home cooked meals and the home brewed beers whenever I needed them. Thanks to Leah for being there to listen to me on the walk home. Thanks to all my ocean friends, the LSC was bearable with all of you to endure it with. Thanks to all my friends in Woodstock, Halifax and around the world. You guys will never know how much I appreciate you.

My greatest thanks of all goes out to the people who made the *CCGS Amundsen* my favourite place to be. Thank you to each and every person I have been on board with for making my time at sea the best adventure I have been on. I never could have imagined when this journey began that I would spend almost 200 days at sea with some of the greatest people I have ever met. Being on board with all of you has been my favourite time.

CHAPTER 1: INTRODUCTION

1.1 Motivation

A large addition of carbon dioxide (CO_2) to the atmosphere from anthropogenic sources has taken place since the beginning of the industrial revolution (*Keeling et al*., 1976). An increase in atmospheric CO_2 ultimately has two effects, increasing the temperature of the Earth and atmosphere, as well as contributing to ocean acidification when it is absorbed by the ocean. The ocean has taken up approximately one third of the anthropogenic CO_2 emitted to the atmosphere (*Ciais et al*., 2013). Once in the ocean, the transport of dissolved CO_2 into deep basins allows for long-term storage of this climate active gas. In coastal regions, the exchange of CO_2 between the atmosphere and the ocean is more complex, yet more poorly quantified than in the open ocean.

Coastal and shelf seas are dynamic areas where the oceanic, terrestrial, and atmospheric carbon reservoirs interact. These areas are influenced by the high input of nutrients and carbon from riverine and atmospheric sources as well as by upwelling and physical mixing. Although the total area of continental shelves is small compared to that of the global ocean, elevated levels of primary production and carbon cycling take place here, making them globally important for the exchange of CO_2 (*Gattuso et al*., 1998). Shelf seas can act as strong sources or sinks of CO_2 depending on a variety of factors. The contribution of shelf seas to the global ocean carbon sink is not well constrained and differs strongly between regions (*Borges*, 2005). Shelf seas in the Arctic Ocean are expected and shown to be strong sinks of CO_2, but quantification of these sinks is not well documented. Changes in the Arctic are greatly affecting carbon inputs and cycling

on the shelves (e.g., *Bates*, 2006; *Shadwick et al*., 2011a; *Else et al*., 2013; *Anderson & Macdonald*, 2015). Arctic shelves are expected to be more sensitive than temperate regions to climate change due to faster warming of the shallow water column, fewer trophic links in local ecosystems (*Carmack and Wassmann*, 2006), a relatively low alkalinity, and a weak carbonate buffering capacity (*Shadwick et al*., 2013).

Alterations of the environment caused by changes in global climate are strongest in the Arctic. Air temperatures in the Arctic have increased more than twice as fast as the global average (*Cohen et al*., 2014). The summer extent of sea-ice in the Arctic Ocean has decreased by 50% since the earliest satellite records in 1979 (*Barber et al*., 2015). Increased precipitation along drainage basins has caused an increase in freshwater discharge by rivers and a subsequent alteration in the export of terrestrial carbon and suspended load transport (*Carmack and Wassmann*, 2006; *Doxaran et al*., 2015). These environmental changes cause a multitude of alterations in physical processes, ecosystem structure, and biogeochemical cycles within the Arctic Ocean. Primary production is altered by increased light availability, temperature changes, freshwater input, nutrient fluxes, and source water composition among other factors. Increased open water allows for greater wind forcing, ultimately changing currents and upwelling dynamics on the shelves. These processes have confounding effects on the marine inorganic carbon cycle and make it difficult to predict the response of the Arctic Ocean to future change.

1.2 The Global Carbon Cycle

The carbon cycle involves the exchange and transformation of carbon through the Earth system. It plays a large role in controlling global climate by regulating the amount of CO_2 in the atmosphere. The main reservoirs or pools of carbon are the atmosphere,

terrestrial biosphere, oceans, and sediments (including fossil fuels and carbonate rocks). Biological, chemical, and physical processes transfer carbon between different reservoirs on varying time scales. Carbon dioxide is transferred from the atmosphere to the ocean by gas exchange, and from biota to other reservoirs through photosynthesis and respiration. The global carbon budget is a balance of the exchanges between reservoirs. In pre-industrial times, the budget was roughly in steady state, with all flux terms balancing each other in total (*King et al*., 2007). The anthropogenic addition of CO_2 to the atmosphere through the burning of fossil fuels, land use change, and agricultural practices has upset this balance. This large addition exceeds the natural variation in atmospheric CO_2 concentration and cannot be balanced by the natural biological and physical processes that remove CO_2 from the atmosphere due to the vastly different time scales of the processes (*King et al*., 2007).

The ocean contains the largest pool of available, actively cycled carbon. Gas exchange between the ocean and the atmosphere is dependent on the concentration of CO_2 in each medium, as well as temperature, wind speed, sea surface roughness, and ocean circulation. Rivers also play a large role in delivering carbon from land to the ocean reservoir in the form of dissolved inorganic carbon (DIC), particulate carbon and alkalinity (TA). Once in the ocean system, inorganic carbon is taken up by phytoplankton to produce particulate organic carbon (POC). Transportation to the deep ocean is the result of physical mixing or sinking of detritus and allows for the storage of carbon over longer time periods before being buried in sediments or brought back to the surface as respiratory DIC by mixing. The ocean contains approximately fifty to sixty times more CO_2 than the atmosphere (*Ciais et al*., 2013), making it a major regulator of atmospheric CO_2 concentration, meaning a small change in the ocean cycling of carbon could cause

large changes in atmospheric concentrations. Ocean cycling of CO_2 must be accurately understood to determine past, present, and future effects of this greenhouse gas on atmospheric temperature and ocean acidification.

1.3 Carbonate Chemistry

The ocean is a large reservoir of carbon in the global cycle. The ocean and atmosphere exchange carbon in the form of CO_2. When CO_2 enters the ocean, it reacts according to the following equilibrium equations:

$$CO_2 + H_2O \leftrightarrow H_2CO_3 \quad (1.1)$$

$$H_2CO_3 \leftrightarrow H^+ + HCO_3^- \quad (1.2)$$

$$HCO_3^- \leftrightarrow H^+ + CO_3^{2-} \quad (1.3)$$

Carbon dioxide is present in the ocean in four forms: aqueous carbon dioxide (CO_2), carbonic acid (H_2CO_3), bicarbonate (HCO_3^-), and carbonate ion (CO_3^{2-}). Carbonic acid is unstable and so the dissociation to H^+ and HCO_3^- as shown in Eq. 1.2 is favoured. The quantity of carbonic acid present in seawater is usually included in the parameter CO_2^*:

$$[H_2CO_3] + [CO_2] = [CO_2^*] \quad (1.4)$$

The most abundant form of dissolved inorganic carbon in the ocean is HCO_3^-, with CO_3^{2-} and CO_2^* making up the rest. Equilibrium relationships between the concentrations of carbonate species can be written:

$$K_0 = \frac{[CO_2^*]}{fCO_2} \quad (1.5)$$

$$K_1 = \frac{[HCO_3^-][H^+]}{[CO_2^*]} \quad (1.6)$$

$$K_2 = \frac{[CO_3^{2-}][H^+]}{[HCO_3^-]} \quad (1.7)$$

where the equilibrium constants depend on temperature, pressure and salinity, and K_0 is the Henry's Law constant. fCO_2 is the fugacity of CO_2 in units of μatm. The fugacity of CO_2 can be used to compute the partial pressure of CO_2 (pCO_2) using a correction for non-ideal gas behaviour:

$$fCO_2 = \gamma pCO_2 \quad (1.8)$$

where γ is the fugacity coefficient which varies from 0.996 at 0 °C to 0.997 at 30 °C (*Zeebe and Wolf-Gladrow*, 2001).

The individual concentrations of carbonate species in seawater cannot be measured directly, but there are four measurable parameters that can be used to fully quantify the system. One of these is the fugacity of CO_2, introduced above. Another measurable parameter is the sum of all dissolved species of carbon dioxide, known as the total dissolved inorganic carbon (DIC):

$$DIC = [CO_2^*] + [HCO_3^-] + [CO_3^{2-}] \quad (1.9)$$

Total alkalinity is a near conservative property, meaning it is unaffected by changes in temperature and pressure for these purposes. It can be expressed as the charge balance of the major ions of strong bases (dissociation constant, $pK_a > 4.5$) and acids ($pK_a < 4.5$) in seawater:

$$TA = [Na^+] + 2[Mg^{2+}] + 2[Ca^{2+}] + [K^+] - [Cl^-] - 2[SO_4^{2-}] - [NO_3^-] \quad (1.10)$$

Total alkalinity is further defined with respect to the buffer capacity of seawater by *Dickson* (1981) as the number of moles of hydrogen ion equivalent to the excess of proton acceptors (bases formed from weak acids with dissociation constant $pK_a > 4.5$ at 25 °C) over proton donors (strong acids with $pK_a < 4.5$ at 25 °C) in 1 kg of sample. Using this definition for the major species found in seawater:

$$TA = [HCO_3^-] + 2[CO_3^{2-}] + [B(OH)_4^-] + [OH^-] + [HPO_4^{2-}] + 2[PO_4^{3-}] + [SiO(OH)_3^-] + [NH_3] + [HS^-] - [H^+] - [HSO_4^-] - [HF] - [H_3PO_4] \quad (1.11)$$

Equation 1.11 for total alkalinity is often approximated with the more minor components neglected as:

$$TA \simeq [HCO_3^-] + 2[CO_3^{2-}] + [B(OH)_4^-] + [OH^-] - [H^+] \quad (1.12)$$

The fourth measurable parameter is the total hydrogen concentration, reported as the pH of seawater:

$$pH = -\log [H^+] \quad (1.13)$$

The carbonate system is important for the regulation of pH in the ocean, acting as a buffer against large pH changes due to the addition or removal of CO_2. When an acid is added and produces hydrogen ions, these ions react with CO_3^{2-} to form HCO_3^- (Eq. 1.3), limiting the change in pH. This buffering capacity is reduced as more CO_2 is added to the ocean. The ability of seawater to buffer the addition of CO_2 is expressed by its Revelle Factor:

$$Revelle\ Factor = \frac{\Delta[\rho CO_2]/[\rho CO_2]}{\Delta[DIC]/[DIC]} \quad (1.14)$$

The Revelle Factor quantifies the relative change in seawater pCO_2 for a given relative change in DIC. It is proportional to the ratio of DIC to TA in seawater (*Broecker et al*., 1979). A low Revelle Factor indicates a high buffering capacity and vice versa. High latitude regions like the Arctic Ocean have high Revelle Factors and so a weak buffering capacity for added CO_2 (*Orr et al*., 2005).

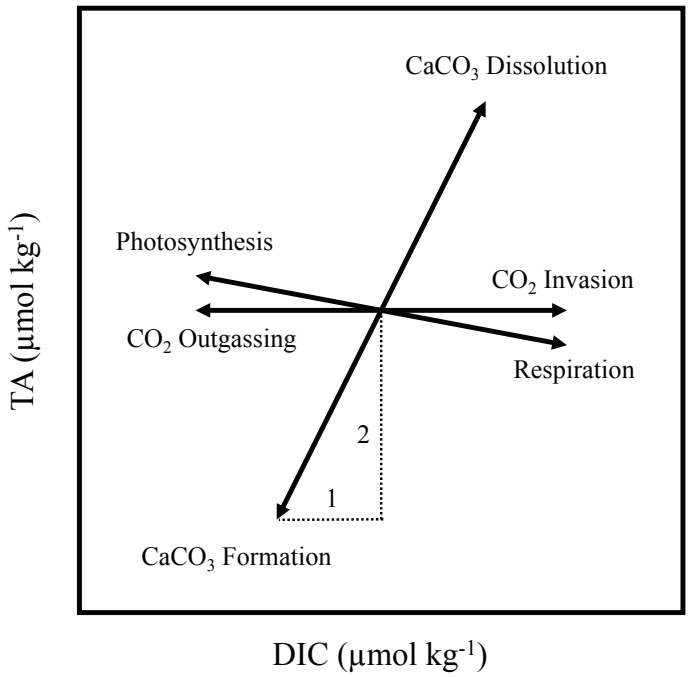

Figure 1.1: Schematic diagram of the effect of processes on TA and DIC concentrations, shown by arrows.

Several processes, illustrated in Figure 1.1, cause changes in the DIC and TA of seawater. The absorption of CO_2 from the atmosphere increases the DIC but has no effect on TA as the resulting H_2CO_3 dissociates to form H^+ and HCO_3^- (Eq. 1.2) and so the total charge remains unchanged. This process also decreases the pH of sea water due to the production of H^+. The release of CO_2 from the ocean has the opposite effect on each parameter. Photosynthesis and respiration alter DIC through the biological uptake or release of CO_2 in water. These processes also change TA to a lesser degree. When NO_3^- is

taken up by marine organisms TA increases whereas the release of inorganic nitrogen by remineralization decreases TA (Eq. 1.10). TA and DIC are also affected by the precipitation of calcium carbonate ($CaCO_3$) by organisms such as coccolithophores, forminifera, pteropods, and corals, and the dissolution of these calcareous shells and skeletons. Dissolution of 1 mole of $CaCO_3$ (resulting in Ca^{2+} and CO_3^{2-} ions) increases TA by 2 moles (Eq. 1.11) and increases DIC by 1 mole (Eq. 1.9).

The chemical stability of calcium carbonate in the ocean is determined in part by the calcium carbonate saturation state of sea water, which is partially a function of the carbonate ion concentration. The calcium carbonate saturation state (Ω) is expressed as:

$$\Omega = \frac{[Ca^{2+}] \times [CO_3^{2-}]}{K_{sp}^*} \tag{1.15}$$

where K_{sp}^* is the stoichiometric solubility product at in-situ temperature, salinity, and pressure. Values of $\Omega > 1$ correspond to supersaturation of $CaCO_3$, or potential formation of calcium carbonate. Values of $\Omega < 1$ correspond to undersaturation, or potential dissolution of calcium carbonate. Undersaturation of aragonite and calcite is corrosive to calcifying organisms such as bivalves, mollusks, and echinoderms that produce $CaCO_3$ as structural components such as shells or skeletons (*Ries et al*., 2011). This can have negative impacts on community structure and recruitment, possibly impacting higher trophic levels (*Fabry et al*., 2008). As CO_2 is added to the water column, pH is reduced by the addition of H^+ ions (Eq. 1.2) and the calcium carbonate saturation state is lowered by the removal of CO_3^{2-} ions through the buffering effect (Eq. 1.3). This process of decreasing pH through the addition of CO_2 and the negative consequences for the carbonate saturation state is known as ocean acidification (OA).

Using two of the measureable carbonate system parameters (DIC, TA, fCO_2, pH) and knowing salinity, temperature and pressure of the water sample, all other parameters and related carbonate system values can be calculated. In this study, DIC and TA were measured and the unknown parameters were computed using the equations given above with the use of the *CO_2Sys* program of *Lewis and Wallace* (1998), using the equilibrium constants of *Mehrbach et al.* (1973) refit by *Dickson and Millero* (1987).

1.4 Stable Isotope Fractionation

Stable isotopes of an element have the same atomic number, and so the same chemical properties, but different atomic masses. In light elements where the relative mass difference is significant between isotopes, isotopic fractionation can cause differences in the relative amount of each isotope between phases or regions. The delta (δ) notation is used to represent isotopic ratios:

$$\delta = \frac{R_{sample} - R_{standard}}{R_{standard}} \times 1000\ ‰ \qquad (1.16)$$

where R is the ratio of the heavy isotope to the lighter isotope and δ represents the relative difference in parts per thousand (‰). In this study, measurements of the carbon isotope ratio of inorganic carbon (δ^{13}C-DIC) and the oxygen isotope ratio of water (δ^{18}O) are used to analyze certain biological and physical processes. The processes that lead to the fractionation of $^{13}C/^{12}C$ and $^{18}O/^{16}O$ are discussed further below.

1.4.1 $\delta^{13}C$ of Dissolved Inorganic Carbon

The $\delta^{13}C$-DIC in water samples is used to investigate the role of biological production on the uptake and transfer of inorganic carbon to depth. A preferential uptake of the lighter ^{12}C relative to the heavier ^{13}C isotope during biological production leads to a fractionation of the $^{13}C/^{12}C$ isotopes in both the organic matter and the water. This results in an enrichment of the heavier isotope in the high productivity surface waters. As organic matter sinks and is remineralized, the lighter ^{12}C isotope is released back to the water column and a depletion of the heavier isotope is observed at depth. The biological processes that alter the distribution of DIC in the water column can therefore be examined using $\delta^{13}C$ measurements.

1.4.2 $\delta^{18}O$ in Sea Water

The value of $\delta^{18}O$ in seawater is used to investigate physical processes in the water column. Different water sources have different values of $\delta^{18}O$ due to the fractionation of $^{18}O/^{16}O$ in H_2O during evaporation and precipitation. The lighter isotope (^{16}O) is more easily evaporated while precipitation tends to release more of the heavier (^{18}O) isotope. This fractionation results in high latitude oceans being more depleted in the heavier isotope compared to lower latitude oceans. Different water masses, precipitation, rivers, and sea-ice melt have known values of $\delta^{18}O$ (e.g. *Cooper et al*., 2008). This allows for the consideration of physical processes such as water mass mixing, freshwater input, and brine formation with changes in the value of $\delta^{18}O$ in water samples.

1.5 The Arctic Ocean

The Arctic Ocean is the most land dominated of the world's ocean basins and comprises around 20% of the world's continental shelves (*Macdonald et al*., 1998). These shallow shelves with less than 200 m water depth cover ~ 36 % of the area of the Arctic Ocean (*Forest et al*., 2015), with centrally located deep basins dominating the remainder. The bottom topography controls much of the circulation (*Dijkstra*, 2008), while connections with other ocean basins are limited. Relatively fresh Pacific water enters the Arctic through the narrow and shallow Bering Strait where it splits in two directions. Part of this Pacific water goes eastward along the Alaskan Shelf and into the Canadian Archipelago; the rest is diverted west into the East Siberian Sea (*Jones et al*., 1998). Warm, salty, Atlantic water enters the Arctic from the surface of the Greenland and Norwegian Seas, through the Fram Strait (*Jones et al*., 1998). Freshwater input has large impacts as the Arctic Ocean receives ~ 10 % of the total global river discharge, resulting in strong estuarine behaviour and high stratification (*Dittmar and Kattner*, 2003).

The Arctic Ocean water column is strongly defined by a consistent layering of water masses. A cold, low-density surface layer results from the mixing of river runoff, sea-ice melt, and low salinity Pacific water (*Rudels et al*., 1996). This freshwater input generates a highly stratified upper water column and limits the depth of winter convection (*Rudels et al*., 1996). The Pacific-origin halocline layer, centred around 100 m depth, is partly the result of dense water formed due to the exclusion of brine during sea ice formation over the shelves (*Aagaard*, 1989). This halocline separates the surface layer from the warmer, more saline Atlantic layer, trapping heat and allowing ice formation to occur (*Jones and Anderson*, 1986). The intermediate temperature maximum due to

Atlantic water below the halocline is maintained throughout the Arctic (*Aagaard et al*., 1985).

Freshwater and sea-ice dynamics in the Arctic Ocean have importance for regional as well as global climate through the alteration of stratification. North Atlantic Deep Water is formed north of the Greenland-Scotland ridge system; the Arctic basins are an important source of dense water to this area that drives global ocean circulation (*Aagaard et al*., 1985). Altered density through changes in freshwater and brine inputs can modify this deep water transport. In addition, surface water and ice exit from the Arctic into these areas of deep water formation and modify surface conditions. A pronounced freshening of this surface water may alter or slow deep water formation by increasing stratification (*Jones et al*., 1998). Modifications of water masses within the Arctic Ocean have far-reaching effects on global circulation and heat distribution.

1.6 The Beaufort Sea

The Beaufort Sea extends from Barrow, Alaska to the southwestern corner of Prince Patrick Island, Canada (Fig. 1.2). It is bordered on the east by Banks Island and to the south by the continental shelves of Alaska and Canada. Water circulation is dominated by the anticyclonic flow of the Beaufort Gyre over the deep Canada Basin (*Carmack et al*., 1989). This wind-driven flow is due to the high-pressure system present over the region in winter (*Barber and Hanesiak*, 2004). The surface circulation is responsible for increases in ice volume as well as the export of ice into the transpolar drift. Surface waters in the Beaufort Sea are a mixture of river discharge, sea-ice melt, and Pacific-origin upper halocline water. Deeper waters, below the highly stratified upper halocline layer are of Atlantic origin. The Beaufort Undercurrent controls the subsurface

waters where flow is reversed in a cyclonic pattern (*Carmack and Macdonald*, 2002). Along the southern boundary, a narrow (15-20 km wide), Pacific-origin, nutrient-rich current, known as the shelf-break jet, flows from the Bering Strait eastward toward the Canadian Archipelago (*Pickart*, 2004).

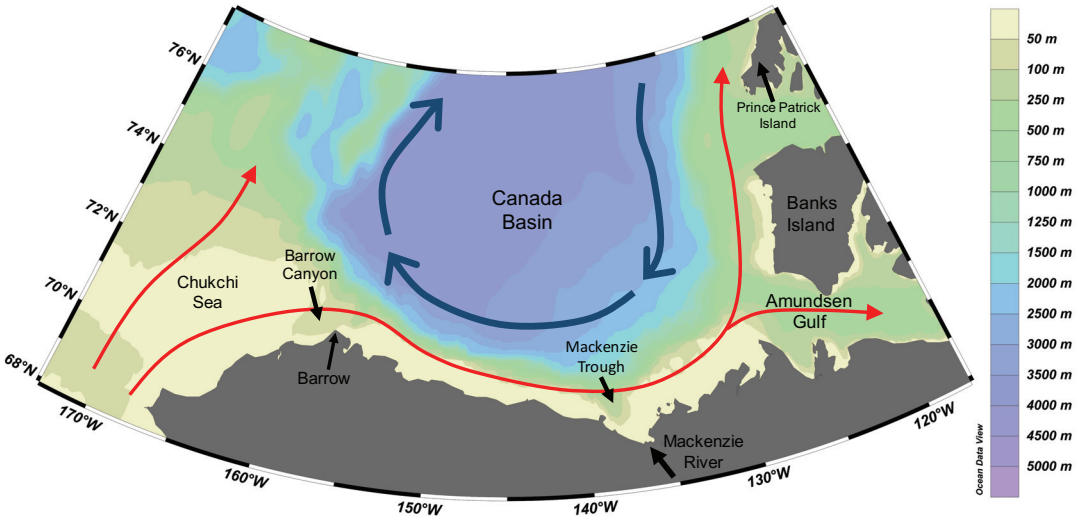

Figure 1.2: Ocean depth (IBCAO, Version 3) and sub-surface circulation in the Beaufort Sea. Red arrows indicate the sub-surface flow of Pacific water entering through the Bering Strait, including the flow of the shelf-break jet. Blue arrows indicate the anticyclonic flow of the Beaufort Gyre. Black arrows indicate river inflow and topographic features.

An anticyclonic water circulation regime with high sea level pressure has been present in the Beaufort Sea since 1997 (*Proshutinsky et al.*, 2015). This anticyclonic rotation leads to an accumulation of low-density water in the Beaufort Gyre and induces a deeper halocline (*Carmack et al.*, 2016). Strong Ekman convergence produces downwelling in Canada Basin and upwelling along the boundary of the Beaufort Sea, contributing to the export of freshwater into the Gyre (*Yang et al.*, 2006). The anticyclonic Gyre exports sea-ice to the south where ice-melt contributes to the freshwater reservoir, enhancing surface stratification over the shelves (*McLaughlin et al.*, 2011). Storms distinct from the prevailing atmospheric flow create upwelling and downwelling on the Beaufort shelves and alter the shelf-break jet. Arctic storms can

accelerate the shelf-break jet and cause downwelling, while Pacific storms or a strong Beaufort High pressure cell cause easterly winds that can reverse the jet and create conditions conducive to upwelling (*Pickart et al*., 2009).

The Beaufort Shelf is an estuarine environment strongly affected by freshwater discharge from the Mackenzie River. The Mackenzie River is the fourth largest river emptying into the Arctic Ocean and the single largest source of sediment to the Arctic Ocean (*Doxaran et al*., 2015). This freshwater discharge takes place year round, with peak flow in early June when warm water and the turbid river plume can spread over several thousand square kilometers (*Doxaran et al*., 2015). Depending on atmospheric and ice forcing, the river plume may be directed northward into the Canada Basin or steered eastward along the coast toward the Canadian Archipelago (*McLaughlin et al*., 2011). The delivery of nitrogen (N) in Mackenzie River discharge has a small to moderate effect on primary production, relieving the N limitation in Beaufort Sea surface waters. This impact is complemented by the upwelling of Pacific water providing nutrients to the lower euphotic zone (*Tremblay et al*., 2014). The Beaufort shelves undergo strong seasonal changes, being ice-free in the summer and mostly ice-covered throughout the winter. Flaw leads and polynyas, such as the Cape Bathurst polynya, play a large role in primary production and carbon dynamics on the shelves, providing an open water environment in winter. These openings in the ice cover provide a location for active ice formation to take place, causing brine enrichment in the water below and dense water formation, resulting in the export of dense bottom water off the shelf (*Backhaus et al*., 1997).

1.7 Shelf-Basin Exchanges

Wind and ice movement are the dominant controls of circulation on the continental shelves of the Beaufort Sea. Shelf-basin exchanges are promoted by upwelling and downwelling induced by surface stress due to wind and ice motion (*Williams et al*., 2006), as well as density driven plumes through canyons, polynya forced spreading, and the instability of boundary currents generating eddies (*Mathis et al*., 2007). Topographic features such as Barrow Canyon, Mackenzie Trough, and Kugmallit Valley, which interrupt the shelf, are areas of enhanced shelf-break exchanges (*Williams et al*., 2006; *Williams et al*. 2008). Advective processes are the main drivers of shelf-basin exchange and halocline ventilation in the Beaufort Shelf region. The shelf-basin pump is one means by which carbon, oxygen and nutrients are transported below the mixed layer and into the permanent halocline for longer-term storage (*MacGilchrist et al*., 2014). This shelf-basin pump is induced by sea-ice formation over the shelves in the fall causing rejection of brine to the water below. This process creates dense water that flows off the shelf in a plume, carrying with it organic matter and remineralization products (*Anderson et al*., 2010).

Sustained periods of westerly winds intensify the eastward flowing shelf-break jet and create conditions for the movement of water and materials to the deep basin. Downwelling (Fig 1.3a) carries particulate and dissolved matter, and remineralization products off the shelf into the deep basin (*Forest et al*., 2007), contributing dense water to the permanent halocline. The westward flowing arm that is part of the Beaufort Gyre is pushed north further away from the shelf-break, allowing water from the shelf out past this point. This creates a scenario in which carbon that has been sequestered by primary production and has sunk beneath the surface mixed layer can be moved from the shelf and

added to the permanent halocline in the basin. Downwelling events are less frequent than upwelling storms, acting to offset on-shelf fluxes, but not reversing the mixing that takes place due to upwelling (*Pickart et al*., 2013).

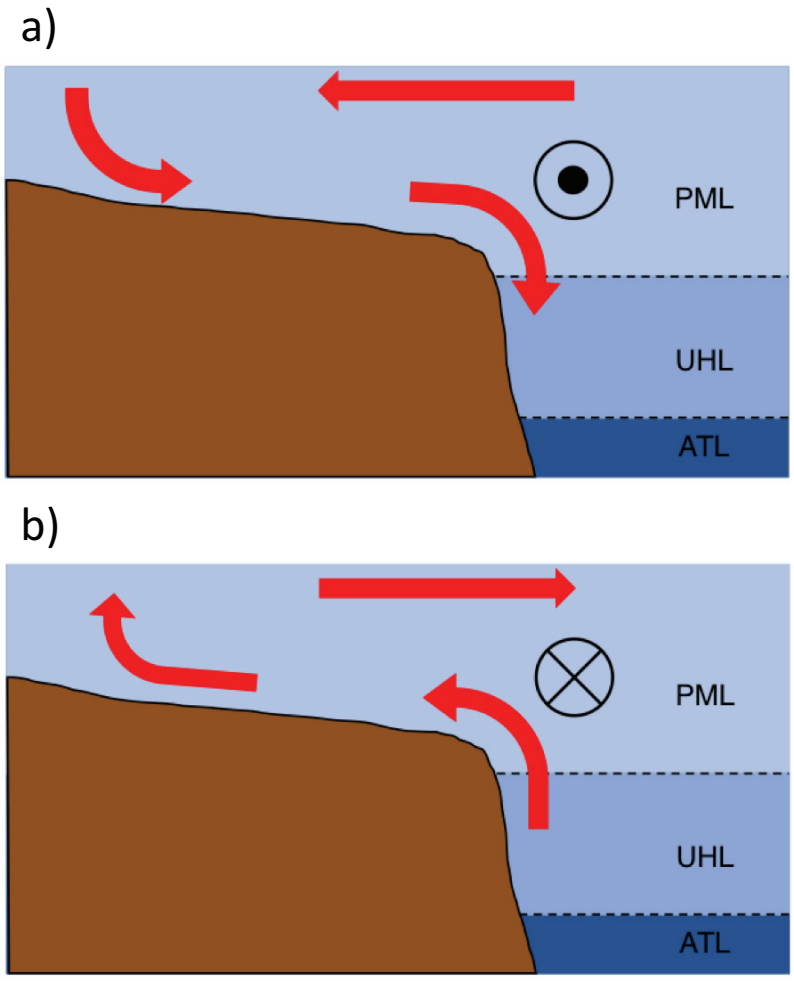

Figure 1.3: Schematic diagrams of a) downwelling and b) upwelling on the Mackenzie Shelf. The direction of the shelf-break jet is indicated in black, red arrows indicate cross-shelf water movement, and water mass layers are identified as PML (polar mixed layer), UHL (upper halocline layer) and ATL (Atlantic layer).

Upwelling (Fig 1.3b) has been well documented on the shelf in the fall when storms are common (e.g. *Mathis et al*., 2012; *Williams and Carmack,* 2015; *Pickart et al*., 2009), and has a variety of effects on the shelf region. Upwelling events provide nutrient-rich, high pCO_2 water to the euphotic zone, increasing primary production (*Williams and*

Carmack, 2015) and altering the source or sink status of shelves in the Beaufort Sea (*Mathis et al*., 2012). Saline water brought onto the shelf in the fall preconditions it for greater amounts of export through brine drainage in the subsequent winter (*Melling*, 1993). Upwelling inducing winds occur throughout the year and so the location of the ice edge is important; if the ice edge is past the shelf-break then intense upwelling can occur that brings water from deeper than the shelf-break (80-100 m) up onto the shelf (*Carmack and Chapman*, 2003) and possibly to the surface where net CO_2 outgassing can occur. If ice cover is present over the shelf, upwelling can still occur, but the high pCO_2 water is capped from the atmosphere and light for biological production is limited. Upwelling and offshore Ekman transport on the shelf also causes downwelling in the Beaufort Gyre, increasing freshwater content, deepening the nutricline, and decreasing productivity in this area (*McLaughlin et al*., 2011).

With changing sea-ice cover, freshwater input, and wind forcing, the already complex cycling of carbon on the shelves of the Beaufort Sea is becoming more important to monitor and study.

1.8 Thesis Objectives

1. Characterize and investigate the carbonate system in the southeastern Beaufort Sea in the fall of 2014.
2. Quantify the along-shore volume transport on the Mackenzie Shelf to investigate its relationship to wind forcing and cross-shelf upwelling and downwelling circulation.
3. Quantify cross-shelf fluxes of inorganic carbon on the Mackenzie Shelf to better constrain carbon transfer onto the shelf due to upwelling.

CHAPTER 2: METHODS

This chapter gives a detailed description of the methods used in the following research. The collection of water samples is overviewed and the methods for determination of DIC and TA explained. The use of a three-end member mixing scheme to perform a water mass decomposition is described. Details of the Arctic and Northern Hemisphere Atlantic (ANHA) simulation are introduced and the methods for working with the simulation velocity field output are outlined.

2.1 Collection and Analysis of Carbonate Parameters

Water samples were collected during an expedition from August 17th to September 21st of 2014 onboard the *CCGS Amundsen*. A total of 23 stations (Fig. 2.1) were sampled over the entire water column for DIC, TA, δ^{13}C-DIC, and δ^{18}O isotopes. Water samples for the analysis of DIC and TA were collected from the rosette into 250 mL borosilicate glass bottles with stoppers; a supersaturated solution of mercuric chloride ($HgCl_2$) was added to halt biological activity. Samples were stored at 4°C in the dark to await analysis. DIC and TA were analyzed using a VINDTA 3C (Versatile Instrument for the Determination of Titration Alkalinity, by Marianda). Details on the methods for determination of DIC and TA, following *Dickson et al*. (2007), are given below. Water samples for the measurement of δ^{13}C-DIC and δ^{18}O were collected in tandem with DIC and TA samples from the rosette. δ^{13}C-DIC samples were analyzed at the Yale Analytical and Stable Isotope Center (Yale University) using a GasBench II system connected to a Thermo Delta Plus XP isotope ratio mass spectrometer. δ^{18}O samples were analyzed by

isotope ratio mass spectrometry at GEOTOP Stable Isotope Laboratory (University du Quebec à Montréal).

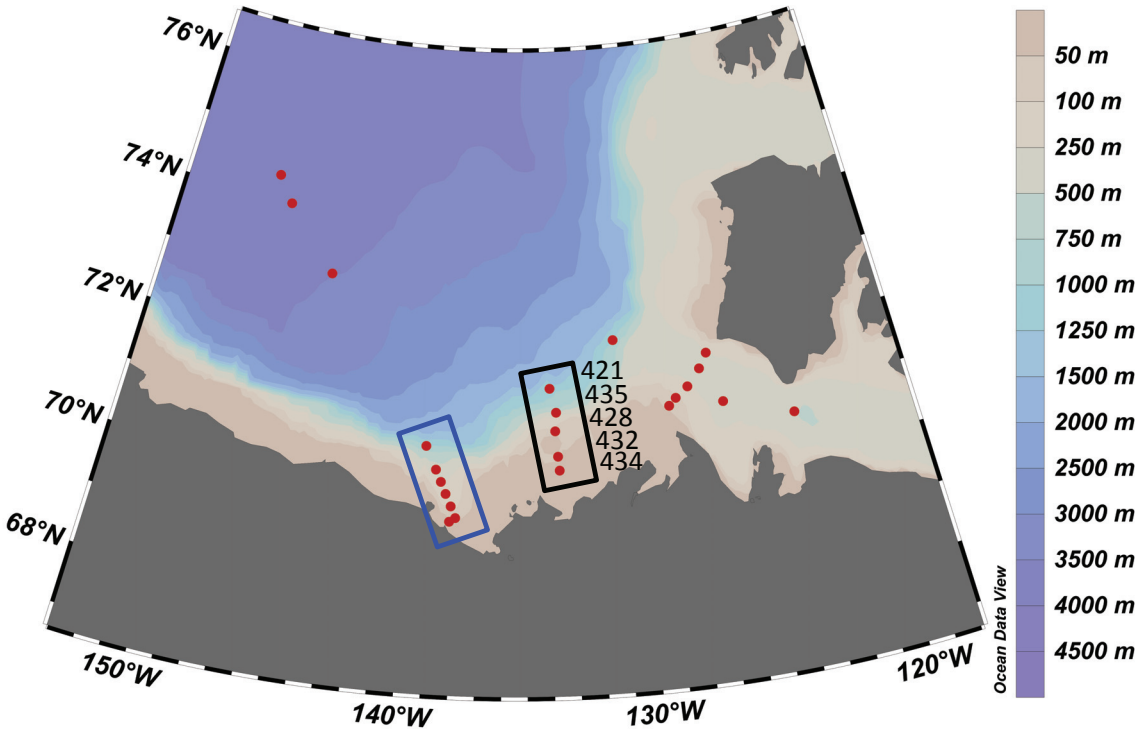

Fig. 2.1: Map of stations (red dots) sampled in the Beaufort Sea during August and September of 2014. The black rectangle signifies the stations that make up the Mackenzie Shelf transect with numbers indicating station names. The blue rectangle signifies stations that make up the Mackenzie Trough transect.

2.1.1 Dissolved Inorganic Carbon

Coulometric titration is the method used in determining DIC. A defined volume of seawater is delivered to a glass stripping chamber along with a small volume of phosphoric acid (8.5% H_3PO_4). The strong acid reacts with all the carbonate species present to form CO_2, which is stripped from the sample by bubbling a CO_2 free carrier gas (N_2) through a glass frit and into the coulometer cell.

A two-chambered coulometer cell is used. The primary chamber is filled with 100 cm^3 of cathode solution (UIC Inc.) containing ethanolomine as the reactive agent, dimethyl sulfoxide (DMSO), and a pH sensitive dye. The smaller chamber is filled with anode solution containing potassium iodide in DMSO (UIC Inc.) to a level approximately 1 cm lower than the cathode solution. Potassium iodide crystals are added to the bottom of the smaller chamber to ensure that the anode solution remains saturated. The cathode is a platinum (Pt) electrode and the anode is a silver (Ag) electrode.

The CO_2 extracted from the sample is added to the absorbent solution in the coulometer cell, where the ethanolomine reacts with the CO_2 to form hydroxyethylcarbamic acid:

$$CO_2 + HO(CH_2)_2NH_2 \rightarrow HO(CH_2)_2NHCOO^- + H^+ \qquad (2.1)$$

This reaction results in a colour change due to the presence of the pH indicator. DIC is quantified by the titration of the resulting solution with hydroxide ions:

$$H^+ + OH^- \rightarrow H_2O \qquad (2.2)$$

which are formed from the electrolysis of water:

$$H_2O + e^- \rightarrow \frac{1}{2}H_2(g) + OH^- \qquad (2.3)$$

and silver is oxidized:

$$Ag(s) \rightarrow Ag^+ + e^- \qquad (2.4)$$

Light transmittance is measured in the cell to monitor the colour change. The hydroxyethylcarbamic acid is titrated with OH^- to return the solution back to its original colour. The number of electrons needed to produce the correct amount of hydroxide ions

is measured by the coulometer as the total charge. The quantity of charge measured can then be converted to a molar quantity of DIC using Faraday's second law of electrolysis.

2.1.2 Total Alkalinity

Potentiometric titration is used to determine total alkalinity. A peristaltic pump is used to deliver seawater to the sample pipette. This seawater is transferred to an open titration cell which is kept at a constant temperature of 25°C by a circulating water bath. The titration takes place with a solution of hydrochloric acid (HCl) made in a solution of sodium chloride to approximate the ionic strength of seawater. This acid solution is added using a piston burette (Metrohm) in 0.15 mL doses, up to a final volume of 4.20 mL of acid solution. A magnetic stirrer mixes the solution during titration and the pH of the solution is measured after each acid addition. pH is measured as the electromotive force (e.m.f., measured in millivolts) between a pH electrode and a reference electrode. Total alkalinity is then computed by the VINDTA Labview software using a modified Gran approach (*Dickson et al*., 2007).

2.1.3 Calibration With Reference Material

Certified Reference Materials (CRMs) with precisely determined values of DIC and TA are provided by A. G. Dickson (Scripps Institute of Oceanography). These CRMs are run using the same methods for DIC and TA as noted above at the beginning and end of each sample measurement period. Deviations from these certified values are used to calibrate the sample values. This routine CRM analysis ensures that the uncertainty in the DIC and TA measurements is less than 2 μmol kg^{-1} and 3 μmol kg^{-1} respectively.

2.2 Water Mass Definitions

The distribution and vertical structure of water masses in the Arctic Ocean is well known and documented (e.g., *Jones and Anderson*, 1986; *Aagaard*, 1989; *Swift et al*., 1997; *Jones et al*., 1998). The variable influence of freshwater from rivers and sea-ice melt has large implications for stratification and circulation (e.g., *Aagaard and Carmack*, 1989; *Rabe et al*., 2011; *McClelland et al*., 2012). Various schemes have been used to classify and name the different major water masses. In this study, the vertical water column is divided into three major water masses. At the surface is the polar mixed layer (PML), a mixture of meteoric water (MW), sea-ice melt (SIM) and upper halocline Pacific-origin water. The upper halocline layer (UHL) lies below the PML, centered around 100 m depth and displaying a subsurface temperature minimum. Below the UHL is the Atlantic layer (ATL), characterized by an increase in temperature and a salinity maximum.

Using a three end-member mixing scheme allowing for negative values, assuming conservative mixing, and knowing the TA and $\delta^{18}O$ of all water masses, the relative fraction of water masses in a sample with known TA and $\delta^{18}O$ can be calculated. This technique has been shown successful through multiple independent studies in the same geographic area as is presently investigated (e.g., *Yamamoto-Kawai et al*., 2009; *Shadwick et al*., 2011b). The upper 150 m of the water column is assumed to be a mixture of MW, SIM, and UHL, and the following system of equations is solved for the relative fraction of each:

$$f_{MW} + f_{SIM} + f_{UHL} = 1 \quad (2.5)$$

$$TA_{MW}f_{MW} + TA_{SIM}f_{SIM} + TA_{UHL}f_{UHL} = TA \quad (2.6)$$

$$\delta^{18}O_{MW}f_{MW} + \delta^{18}O_{SIM}f_{SIM} + \delta^{18}O_{UHL}f_{UHL} = \delta^{18}O \quad (2.7)$$

where f_x represents the relative fraction of each water mass. Below 150 m, the water is assumed to be a mixture of net SIM, UHL, and ATL, and the following system of equations is used:

$$f_{SIM} + f_{UHL} + f_{ATL} = 1 \quad (2.8)$$

$$TA_{SIM}f_{SIM} + TA_{UHL}f_{UHL} + TA_{ATL}f_{ATL} = TA \quad (2.9)$$

$$\delta^{18}O_{SIM}f_{SIM} + \delta^{18}O_{UHL}f_{UHL} + \delta^{18}O_{ATL}f_{ATL} = \delta^{18}O \quad (2.10)$$

The end-member values used for each water mass are shown in Table 2.1. The TA value for MW is the flow-weighted value of Mackenzie River water taken from *Cooper et al*. (2008). The $\delta^{18}O$ value for MW is a flux-weighted value for the Mackenzie River taken from *Yi et al*. (2012). These endmembers give a balanced value for the river water endmember throughout the year. Although Alaskan and Eurasian rivers may have some influence on the upper water column in this area and contribute water with different properties, the dominant input of MW to the study area is the Mackenzie River and so these values are used. The value of $\delta^{18}O$ for SIM is taken from *Yamamoto-Kawai et al*. (2009), and the value of TA for SIM is taken from *Lansard et al.* (2012). Values of $\delta^{18}O$ and TA for UHL are taken as the average values of all water samples at a salinity of 33.1, considered to be the core of the UHL water mass. ATL values are similarly the average of all values at the deep temperature maximum, also further characterized by a salinity of 34.8.

Table 2.1: End member water mass properties used in the three component mass balance equations.

Water Mass	Salinity	$\delta^{18}O$ (‰)	TA (μmol kg^{-1})	DIC (μmol kg^{-1})	DIC/TA
MW	0	-19.1	1540	1390	0.90
SIM	0	-2.0	415	330	0.80
UHL	33.1	-1.4	2276	2226	0.98
ATL	34.8	0.18	2302	2167	0.94

2.3 Arctic and Northern Hemisphere Atlantic Simulation

The velocity fields used in this study are taken from the ¼ degree Arctic and Northern Hemisphere Atlantic (ANHA4) configuration produced by Paul Myers at the University of Alberta. This is a regional configuration of a coupled ocean-sea ice model, based on the Nucleus for European Modeling of the Ocean (NEMO, Version 3.4) framework (*Madec*, 2008). The sea-ice model used is the Louvain La-Neuve Sea-Ice Model Version 2 (LIM2) with an elastic-viscous-plastic (EVP) rheology, including both thermodynamic and dynamic modules (*Fichefet and Maqueda*, 1997). The horizontal mesh is a subdomain of the global ORCA025 tripolar grid with two open boundaries, one close to the Bering Strait in the Pacific Ocean and the other at 20 °S in the Atlantic Ocean. In the vertical, there are 50 unequally spaced geopotential levels with high resolution (~ 1 m) focusing on the top 10 m.

This simulation is integrated from January 2002 to December 2014. The initial conditions (3D temperature, salinity, horizontal velocities, sea surface height and sea ice) are extracted from the Global Ocean Reanalysis and Simulations (GLORYS2v3) produced by Mercator Ocean (*Masina et al*., 2015). Hourly 33 km resolution atmospheric forcing data (10 m wind, 2 m air temperature and humidity, downwelling and longwave radiation flux, and total precipitation) from the Canadian Meteorological Centre (CMC)

global deterministic prediction system (GDPS) reforecasts (CGRF) dataset (*Smith et al*., 2014) are used to drive the model. The GLORYS2 dataset is also used to provide the open boundaries (temperature, salinity and ocean velocities). Monthly inter-annual runoff from *Dai et al.* (2009) as well as Greenland meltwater provided by *Bamber et al*. (2012) is also carefully remapped onto the model grid to give a more realistic freshwater input from the land to the ocean. Velocity field output from the simulation was extracted for the current study area and modified for use by Xianmin Hu at the University of Alberta.

2.4 Mackenzie Shelf Transports

Model output gives 5-day averages of the velocity fields in the study area for August and September of 2014. To look at along-shore and cross-shelf transports on the Mackenzie Shelf, the modelled velocity was gridded along the shelf to basin sampled transect (Fig. 2.1) every 5 km, starting from 20 km closer to the shore than the first sampled station and ending ~ 20 km into the basin past the last sampled station. The along-shore direction runs parallel to the shelf-break, at a bearing of 52° to the east of true north (52° T or 232° T). The cross-shelf direction is then 38° to the west of true north (142° T or 322° T). The u and v-components of the modelled velocity from the ANHA4 simulation were tilted to correspond to these bearings, resulting in the u-component of the velocity representing along-shore flow and the v-component representing cross-shelf flow.

Along-shore volume transports were calculated using the tilted u-component of the modelled velocity. The shelf section was defined based on sampled station locations. The Mackenzie Shelf section is 120 km long and goes from close to the shore out to approximately the 200 m isobath. Transport is calculated for the upper 200 m of the water

column by taking the product of the depth-averaged velocity with depth and the cross-shelf area between stations. The along-shore volume transport calculations provide an estimate of total transport. There are errors involved in these calculations due to assumptions and simplifications made. The shelf area that is chosen to calculate the transport over was done so to capture the area that experiences a shift in current direction and to avoid the permanent westward flow of the Beaufort Gyre. The interpolation of modelled velocities to station locations modifies the bottom depths. The actual bottom depth is not used to modify the thickness of the bottom layer at each location. We expect the net effect to be small because the velocity in the bottom layer becomes quite small compared to the mid-depth range of the water column for most of the shelf region. This may change the magnitude, but not the overall direction of the along-shore transport. The along-shore mass transport is used to indicate when cross-shelf fluxes will be the strongest and to identify patterns in the relationship between wind, along-shore, and cross-shelf water movement.

Cross-shelf transports are calculated at the sampled stations on the transects using the v-component of the tilted velocity. Bottom depth is taken from the shipboard depth sounder when sampling took place. Velocity is interpolated only to the station locations where sampling took place and linearly gridded throughout the water column at 1 m intervals. Fluxes are calculated by taking the product of the concentration of the carbonate parameter (e.g. DIC, TA) with the cross-shelf velocity. Mass transports are calculated by taking the sum of the product of the concentration of the carbonate parameter with the cross-shelf velocity, and an along-shore distance of 10 km. Mass per volume for carbonate parameters is calculated by using the UNESCO 1983 (EOS 80) polynomial to determine seawater density (*Fofonoff and Millard*, 1983).

Uncertainty is estimated using Monte Carlo simulations for the calculation of cross-shelf mass transports. The inputs for the simulations were randomly generated from normal distributions and 1000 points were chosen randomly for each of the variables. Standard deviation for salinity, temperature, and DIC measurements were taken directly from sensor or measurement errors. The error of the modelled velocity was estimated by taking the standard deviation of the velocity at each station and model depth layer over the two-month investigation period.

CHAPTER 3: RESULTS & DISCUSSION

3.1 The Beaufort Sea Carbonate System

High variability in the carbonate system properties of surface waters is observed throughout the study region, with marked differences between the basin and distinct shelf regions (Fig. 3.1). Temperature varies from less than -1 °C in the central basin and past the shelf break to greater than 6 °C on the Mackenzie Shelf and in Amundsen Gulf. Salinity ranges from values of less than 26 to greater than 30, with the lowest values in areas close to the Mackenzie River and in the central basin. Higher salinity values in Amundsen Gulf and on the Mackenzie Shelf suggest upwelling of high salinity deep water. DIC at the surface is lowest in waters with low salinity and temperature, primarily in the central basin, and higher in shelf seas, possibly a result of upwelling. TA follows a pattern similar to that of salinity, with low values past the shelf break and in the central basin, and higher values over the shelf. High pCO_2 values are found in waters with high temperature and DIC content, primarily over the shelf and in Amundsen Gulf. The pattern of δ^{13}C-DIC shows lower values over the shelf in areas near the Mackenzie River outflow, possibly due to the more depleted values in river water, while high values of δ^{13}C are found in the north of Amundsen Gulf.

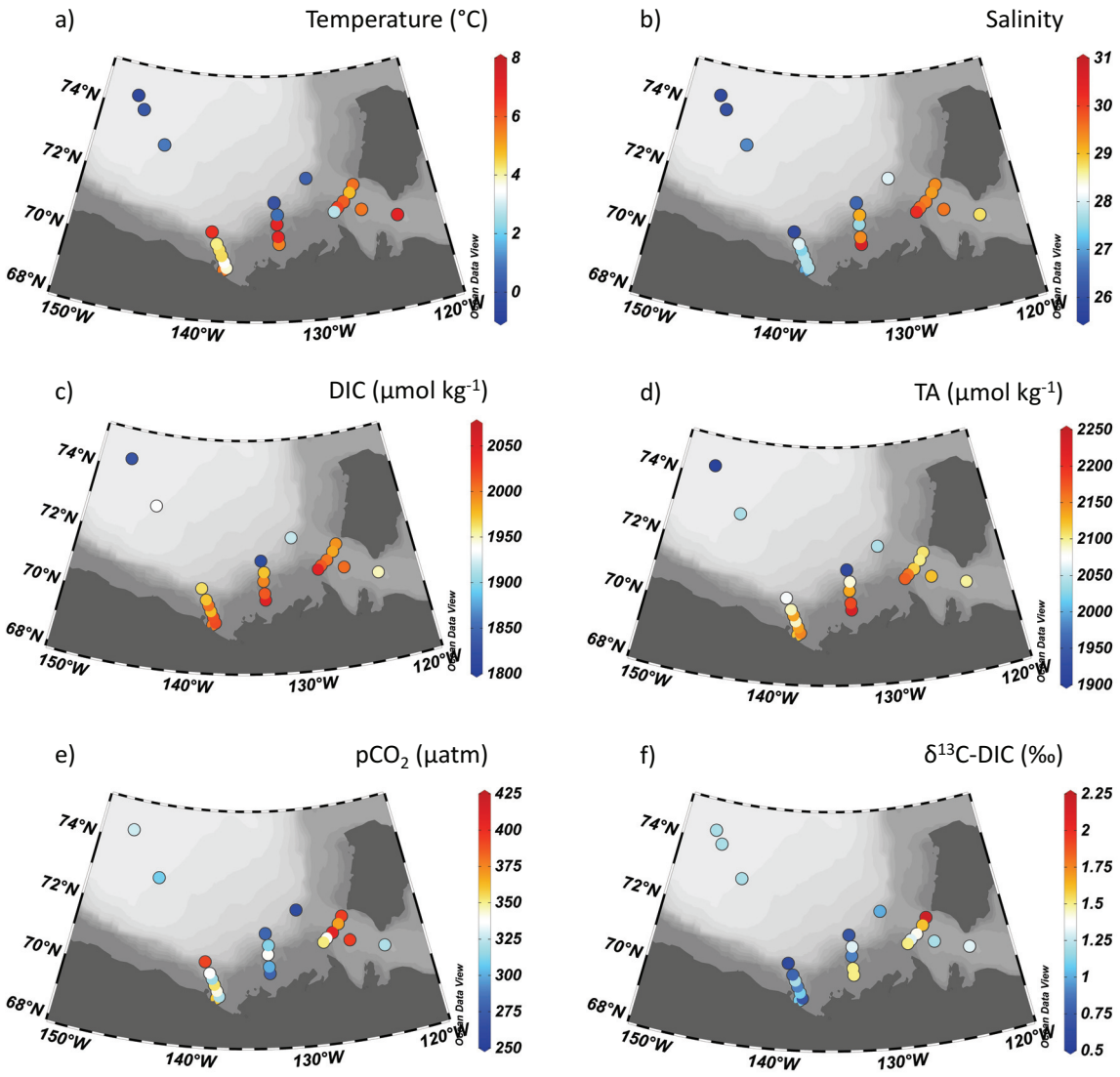

Figure 3.1: Surface properties, a) temperature, b) salinity, c) DIC, d) TA, e) pCO_2, and f) δ^{13}C-DIC, in the study region at each station measured from the surface sample. Samples were taken from August 17th to September 21st.

These surface plots are constructed from surface samples taken over more than a month-long period, from August 17th to September 21st. The stations making up each of the three transects, Amundsen Gulf, Mackenzie Shelf and Mackenzie Trough, were all sampled within a three-day span for each transect, except for the furthest off-shore station on the Mackenzie Trough transect. Possible temporal variability between the three

transects and the stations in the deep basin must be considered when looking at the spatial variability between these areas. Changes in wind and circulation that occurred through the sampling period may alter the surface conditions due to upwelling or downwelling, where the Mackenzie River discharge is directed, and sea-ice concentrations in different areas.

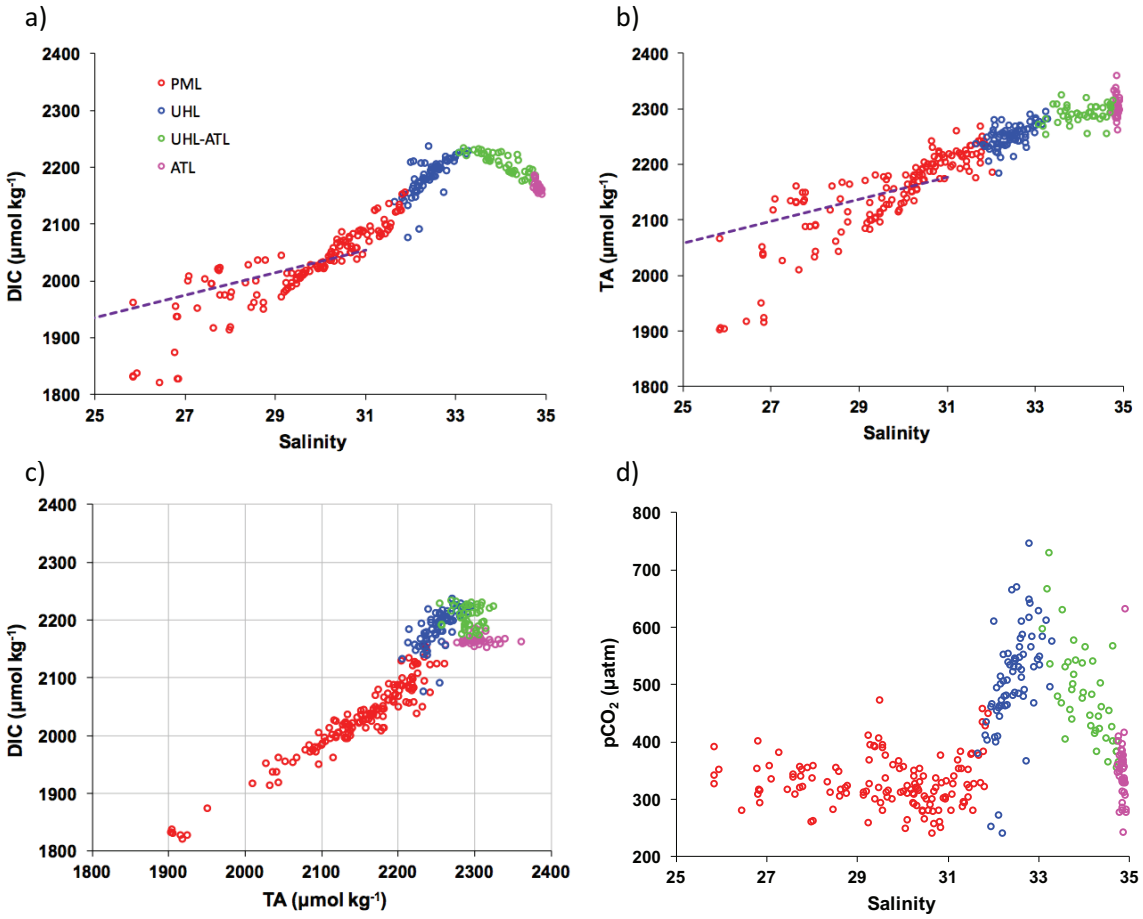

Figure 3.2: a) DIC versus salinity, b) TA versus salinity, c) DIC versus TA, and d) pCO_2 versus salinity for all samples at the stations shown in Figure 2.1. Four water masses are identified by colour: PML (red), UHL (blue), UHL-ATL (green) and ATL (pink). Dashed lines in a) and b) indicate linear regressions to a salinity of zero to find the Mackenzie River end-member of DIC and TA.

Various relationships between DIC, TA, salinity and pCO_2 for all samples on the Mackenzie Shelf, in Amundsen Gulf and in the Canada Basin are shown in Figure 3.2.

DIC and TA are both quite variable in the low salinity PML with the input of freshwater from sea-ice melt and river outflow contributing water with different chemical constituents (Fig. 3.2a and b). DIC ranges widely from 1822 to 2156 μmol kg^{-1} in the PML and TA ranges from 1892 to 2269 μmol kg^{-1} over this same large salinity range of 25.8 to 32.0. DIC reaches a maximum of ~ 2225 μmol kg^{-1} in samples with the maximum fraction of UHL contribution at a salinity of ~ 33.1. This DIC maximum coincident with the maximum fraction of UHL water is regular for this study area. For example, *Shadwick et al.* 2011b found a DIC maximum of 2240 μmol kg^{-1} at the UHL maximum and *Brown et al.* 2016 found a DIC maximum of 2225 ± 8 μmol kg^{-1} at this same salinity horizon. TA shows a maximum of ~ 2360 μmol kg^{-1} in waters with the greatest ATL contribution and a salinity maximum of ~ 34.9. These parameters follow the trends seen in previous years in the same sample areas (e.g. *Shadwick et al*., 2011b).

The relationship between DIC and TA is shown in Figure 3.2c. For samples in the PML the value of the slope of DIC:TA is less than 1, with TA increasing at a faster rate than DIC. TA is mostly conservative while DIC is altered by biological processes, including primary production in the PML. This slope of DIC:TA increases in the UHL to greater than 1, as DIC builds up in the mid-depth layer to its maximum value due to the remineralization of organic matter. A greater value of the DIC:TA ratio indicates that there is respiratory DIC in the water, altering the chemistry and leading to an increase in pCO_2. pCO_2 is variable in the PML, ranging from ~ 200 to 500 μatm, but mostly staying at values below 400 μatm (Fig. 3.2d). The UHL is where pCO_2 reaches its maximum, with values greater than 700 μatm in water associated with the DIC maximum. The UHL is also the layer where the temperature minimum is found. Waters return to the 200 to 500 μatm range in the ATL layer, with a few samples showing increased values. A linear

regression was performed to find the values of DIC and TA at a salinity of zero, representative of the endmember of Mackenzie River water (regression lines shown in Figures 3.2a and b). Only samples in the region with greater than 10 % fMW and less than 5 % fSIM were used for the regression. The resulting endmembers for the values of DIC and TA for the Mackenzie River are 1441 µmol/kg and 1564 µmol/kg respectively. These values are close to the endmembers for the Mackenzie River from *Cooper et al.* (2008) used for the water mass decomposition in this study (Table 2.1).

3.1.1 Mackenzie Shelf Carbonate System

Five stations were sampled from August 22nd to 24th along a transect going across the Mackenzie Shelf, from the shore to beyond the shelf-break (identified in Figure. 2.1). Water properties and carbonate system parameters in the upper 300 m are shown in Figure 3.3. Water temperature is warmest at the surface over the shelf, reaching values of > 6.5 °C. Surface waters over the deep basin are colder, with a maximum temperature of < 1 °C. Salinity, DIC and TA all show similar patterns in the top 300 m over the shelf and beyond the shelf-break. The lowest values (< 26.5, 1830 µmol DIC kg^{-1} and 1920 µmol TA kg^{-1}) are seen in the surface water beyond the shelf-break. Salinity and TA increase down to 300 m, reaching maximum values of approximately 34.8 and 2300 µmol kg^{-1} respectively. DIC has a mid-depth maximum at around 150 m depth of approximately 2225 µmol kg^{-1}, then decreases slightly with depth down to 300 m. All three of these parameters show isoclines sloping up onto the shelf, with equivalent values at shallower depths over the shelf as compared to beyond the shelf-break, as well as elevated surface levels over the shelf. Salinity, DIC and TA reach values of > 32.0, 2200 µmol DIC kg^{-1} and 2270 µmol TA kg^{-1} in the bottom layer at the stations on the shelf.

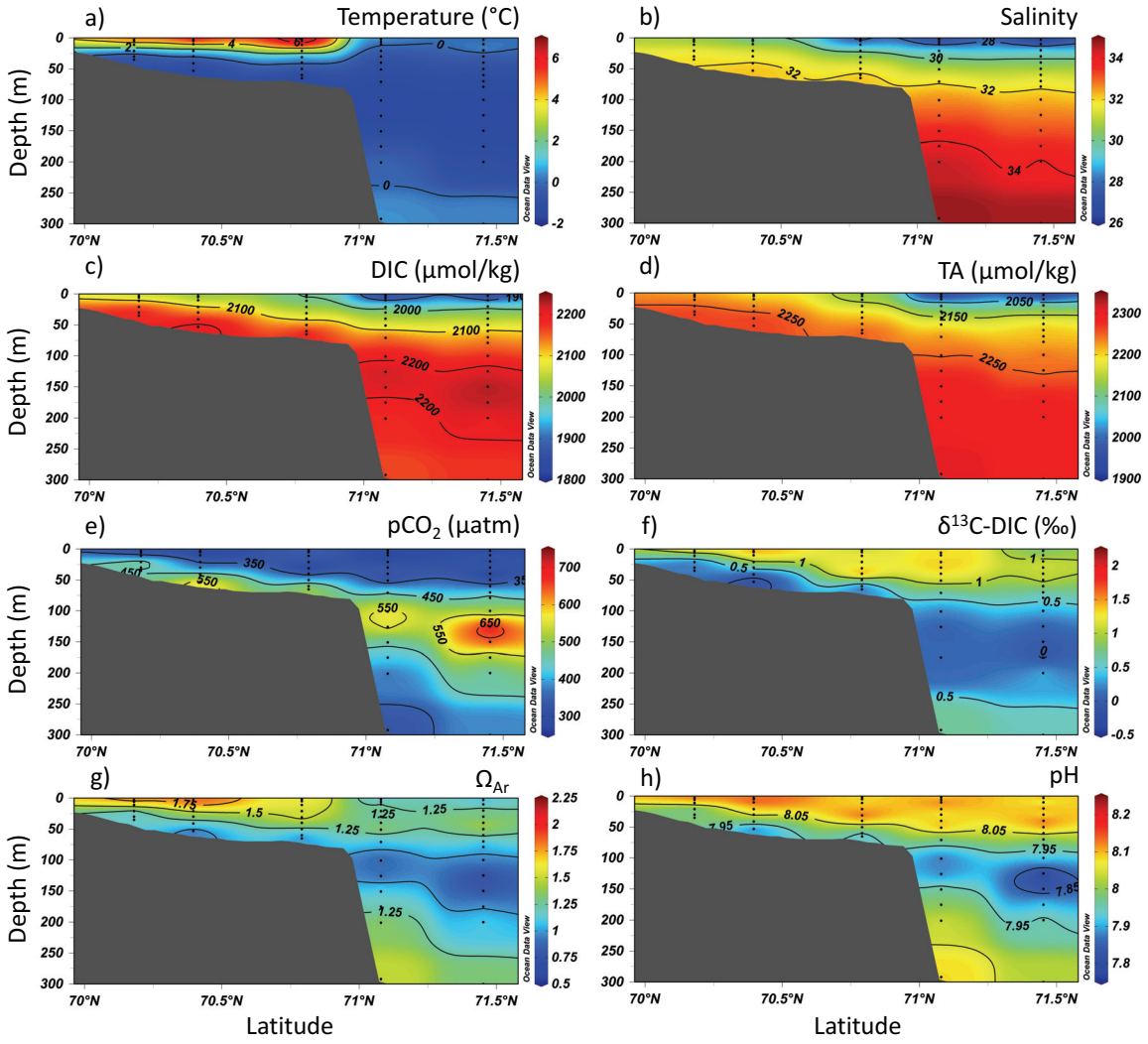

Figure 3.3: Cross-sections of a) temperature, b) salinity, c) DIC, d) TA, e) pCO_2, f) δ^{13}C-DIC, g) Ω_{Ar} and h) pH measured in the top 300 m of the Mackenzie Shelf transect. Measurements are indicated by black dots.

Low values of pCO_2 are present in the surface layer, ranging from 278 to 339 µatm along the transect. Beyond the shelf-break pCO_2 increases with depth to a maximum value of 749 µatm around 120 m depth, located in the UHL (Fig. 3.3e). Below this depth, pCO_2 shows a gradual decrease. Maximum values on the shelf of up to 665 µatm are found in the bottom layer. Measurements of δ^{13}C-DIC show the corresponding pattern, with highest values of up to 2.20 ‰ in the surface or subsurface and a decrease to

minimum values of -0.5 ‰ in the DIC maximum layer over the deep basin and on the shelf bottom. Maximum values of pCO_2 and minimum values of δ^{13}C-DIC are coincident on the shelf bottom and at depths of approximately 120 m past the shelf-break. The temperature effect on pCO_2 is not overly important at these depths, as large changes in temperatures are most prominent in the top 30 m of the water column (Fig 3.3a). Changes in pCO_2 at these greater depths can be attributed more strongly to changes in DIC content, confirmed by changes in values of δ^{13}C-DIC at the same locations. The saturation state of aragonite (Ω_{Ar}) and pH are also closely related to the DIC concentration and pCO_2 levels, with lowest values along the shelf bottom and in the DIC maximum region past the shelf-break. These parameters and the consequences for ocean acidification are discussed further in Section 3.10.

Station 435, on the slope of the Mackenzie Shelf, was sampled on two different dates in 2014, August 22nd and September 23rd. Figure 3.4 shows the profiles of DIC, salinity, temperature and fSIM measured on both sampling dates. The surface properties on August 22nd show lower DIC, salinity and temperature as compared to the second time the station was sampled on September 23rd. These differences in the station properties at the surface most likely come from the increased fraction of sea-ice melt (fSIM) during the first sampling date as compared to the second. It is probable that the sea-ice melt present at the surface over the shelf and slope in late August was moved off the shelf by the end of September. This sea-ice melt effectively dilutes the surface water at station 435, resulting in lower values of Ω_{Ar} and pH (1.07 and 8.069 respectively) as compared to the second sampling date (1.32 and 8.099 respectively).

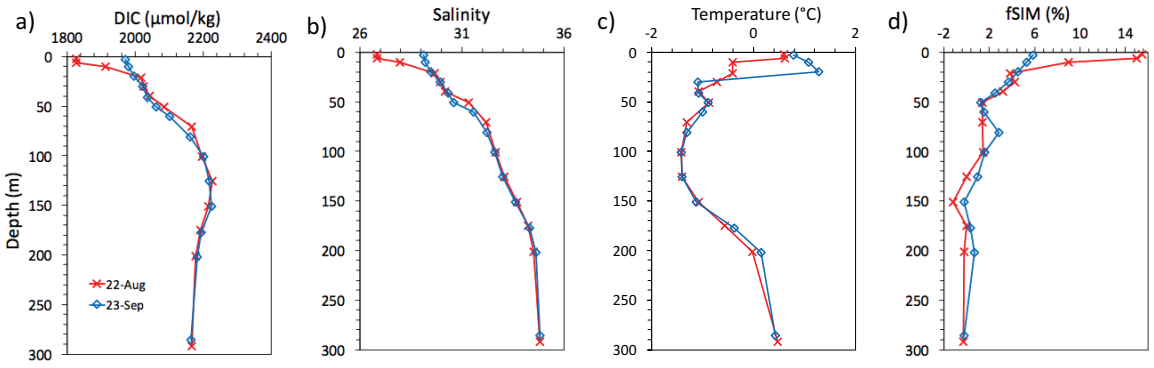

Figure 3.4: Profiles of a) DIC, b) salinity, c) temperature, and d) fSIM at station 435 from two sampling dates, August 22nd (red) and September 23rd (blue).

3.1.2 Mackenzie Trough Carbonate System

Six stations were sampled from September 6th to 7th for physical properties and carbonate parameters through the Mackenzie Trough (Fig. 3.5). Differences in topography and freshwater input alter the observed patterns as compared to the Mackenzie Shelf transect. Temperature is greatest in the surface layer across the whole transect, increasing from the shore (3.78 °C) to a maximum at the deepest station (6.65 °C). Water temperature remains > 3 °C at the station closest to shore all the way down to 42 m depth. At the other stations, temperature declines quickly to a minimum of < -1 °C. The shallowest station in this transect, 470, shows an anomalous pattern of consistent values in all parameters observed as compared to the other stations, remaining at values close to the surface value all the way to the bottom depth (52 m) at the station. Salinity and TA show similar patterns, with low values at the surface and an increase to a maximum at depth. Surface values of salinity and alkalinity show a large range, from 25.8 to 28.0 for salinity and 2067 to 2149 µmol kg^{-1} for TA, increasing and decreasing from station to station with no gradient as seen on the Mackenzie Shelf transect. DIC is also

lowest in the surface layer, with a range in values from 1962 to 2021 µmol kg^{-1}. DIC shows a mid-depth maximum of ~ 2220 µmol kg^{-1} at around 150 m depth.

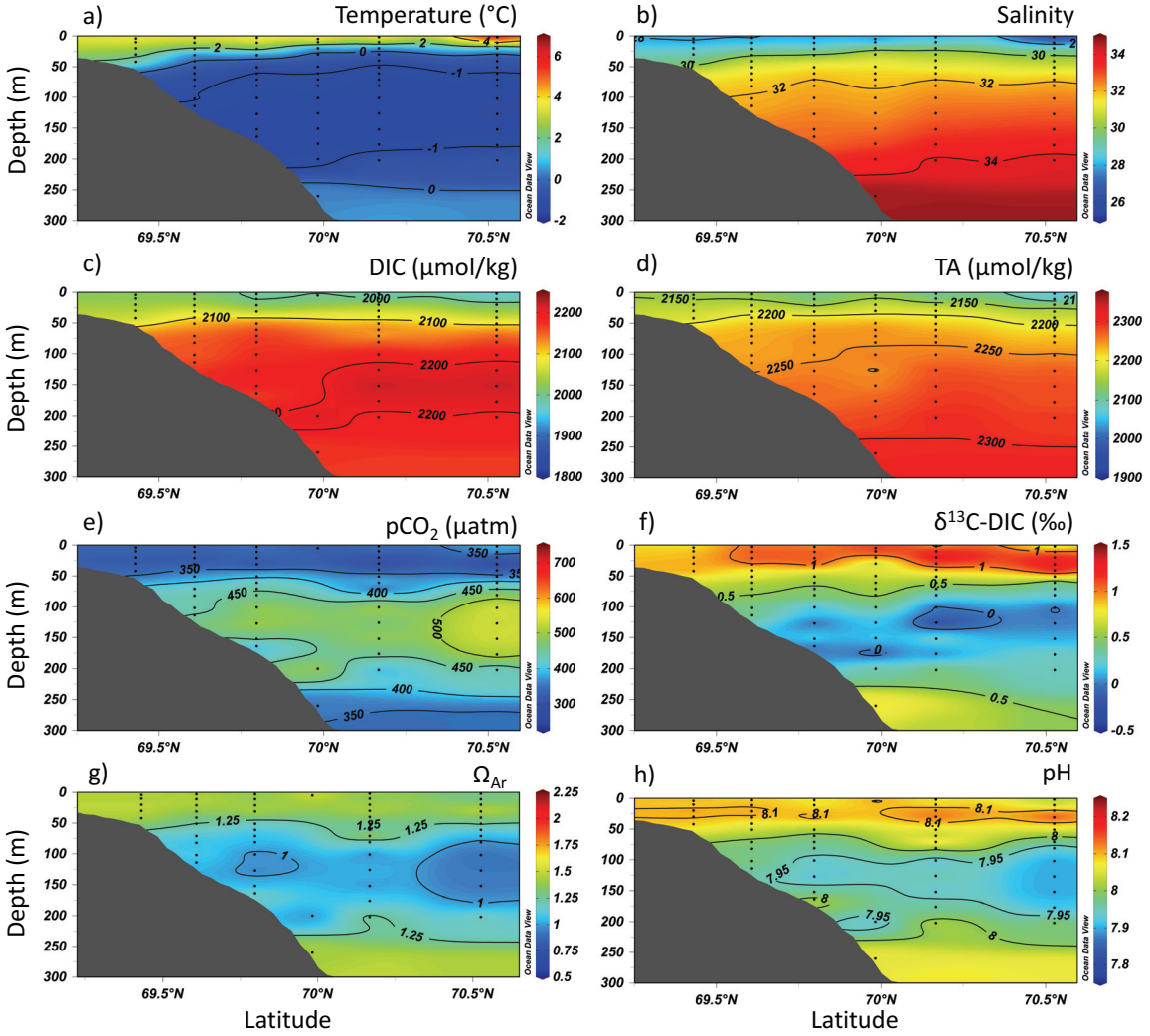

Figure 3.5: Cross-sections of a) temperature, b) salinity, c) DIC, d) TA, e) pCO_2, f) δ^{13}C-DIC, g) Ω_{Ar} and h) pH measured in the top 300 m of the Mackenzie Trough transect. Measurements are indicated by black dots.

Values of pCO_2 remain below 400 µatm in the surface layer, ranging from 316 to 391 µatm. Higher values of pCO_2 are seen at mid-depth from 80 to 200 m, with maximum values at the deepest stations of approximately 530 µatm. Values of δ^{13}C-DIC are highest in the surface, with maximum values of 1.50 ‰ in the top 40 m of the water

column, and decrease to minimum values of -0.40 ‰ in the mid-depth range where the DIC and pCO_2 maxima reside. These low $\delta^{13}C$-DIC values at the same depths as the DIC maximum, where temperature remains quite constant, confirm that changes in the DIC inventory are responsible for changes in pCO_2 at these depths. Minimum values in pH and Ω_{Ar} are present at the same mid-depth range, with the lowest pH of approximately 7.9 at the station furthest offshore. Ω_{Ar} reaches a minimum of 0.89 at this same depth.

3.2 Evidence of Upwelling from Physical Measurements

Carbonate system measurements were taken on the Mackenzie Shelf transect from August 22nd to 24th. Temperature and salinity profiles at the stations on the Mackenzie Shelf are shown in Figure 3.6. The salinity maxima at the bottom of the water column for the shelf stations are compared to where salinity reaches this value at the deep stations to give the effective depth of the shelf bottom waters. The depth of water with the same salinity as the bottom water at stations 434 (45 m), 432 (61 m) and 428 (72 m) is 69, 86 and 90 m at station 435 on the slope and 76, 97 and 101 m at station 421 in the deep basin. Water at these depths is sourced from the UHL, containing DIC and other remineralization products carried off the shelf through various exchange processes. This water is upwelled onto the shelf, altering the composition of the bottom water at these stations. Benthic oxidation due to the sinking of organic matter over the shelf can also be a source of DIC and TA for coastal sites, especially near rivers *(Winde et al*., 2014). Some DIC may be added from local remineralization processes, but there is evidence of transport of UHL water from the deep basin onto the shelf. This upwelling activity increases ocean acidification on the shelf in the bottom waters as well as having implications for air-sea exchange of CO_2 and the sink or source status of the shelf.

Surface water high in meteoric water content is also delivered off shore into the surface layer over the deep basin as upwelling takes place. The effects of upwelling of high UHL water onto the shelf and freshwater transport to the deep basin are discussed further in Section 3.10.

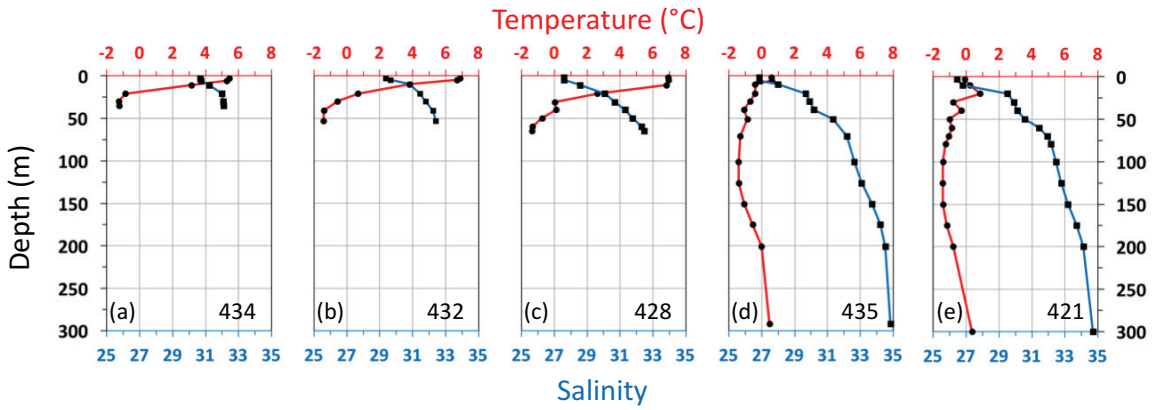

Figure 3.6: Profiles of temperature (red) and salinity (blue) with measurement depths corresponding to carbonate system samples for all stations on the Mackenzie Shelf transect.

Changes in the size and direction of the continental shelf at the Mackenzie Trough create a complicated pattern of circulation and modify the effects of upwelling and downwelling inducing winds. The Trough is a region of enhanced shelf-break exchange due to the convergence of isobaths (*Williams et al*., 2006). There is a greater prominence of upwelling observed in Mackenzie Trough, even with downwelling inducing winds present on the shelf (*Carmack & Kulikov*, 1998). This may cause an increased delivery of halocline water into the Mackenzie Trough, bringing with it nutrients and DIC onto the shelf. It also moves Mackenzie River water away from the estuary and off the shelf into the surface of the deep basin, having consequences for stratification and sea-ice cover. The Mackenzie Trough transect was sampled from September 6th to 7th, except for the deepest station, 482, that was sampled on September 2nd. There is evidence of the suppression of upwelling from salinity and temperature profiles (Fig. 3.7), limiting the

delivery of UHL water high in salinity and DIC content to the shallow shelf stations. Unlike the stations on the Mackenzie Shelf transect, the gradients of salinity do not slope up to lower depths at shallower stations in the Mackenzie Trough. There is also a restriction of water high in pCO_2 and low in pH to depths of greater than 50 m along this transect (Fig. 3.5e and h).

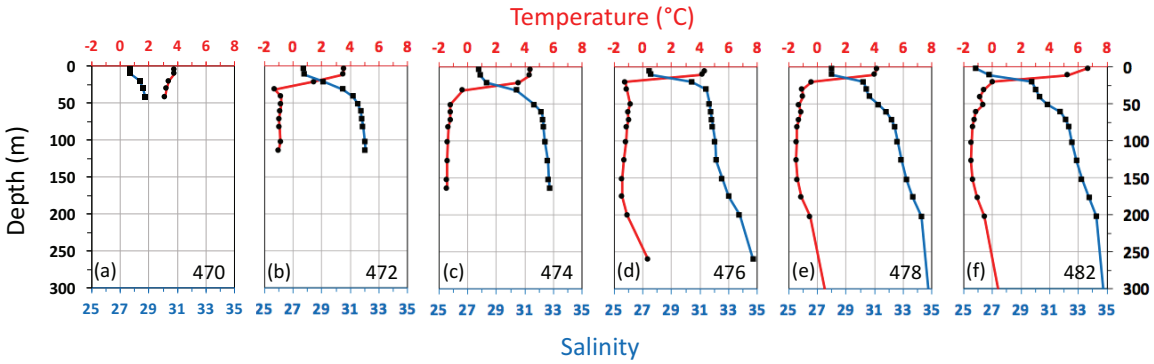

Figure 3.7: Profiles of temperature (red) and salinity (blue) with measurement depths corresponding to carbonate system samples for all stations on the Mackenzie Trough transect.

3.3 Water Mass Decomposition

A decomposition of the water masses in the study region has been completed following the methods described in Section 2.2. Figure 3.8 shows where each water sample plots using the two conservative tracers ($\delta^{18}O$ and TA) in relation to the end-members. The top 100 m of the water column are strongly modified by MW and SIM. The UHL is centred at approximately 100 m depth. A strong mixing line is present between the UHL and the ATL water masses. Some variation in TA is seen in the Atlantic water mass at depths greater than 400 m.

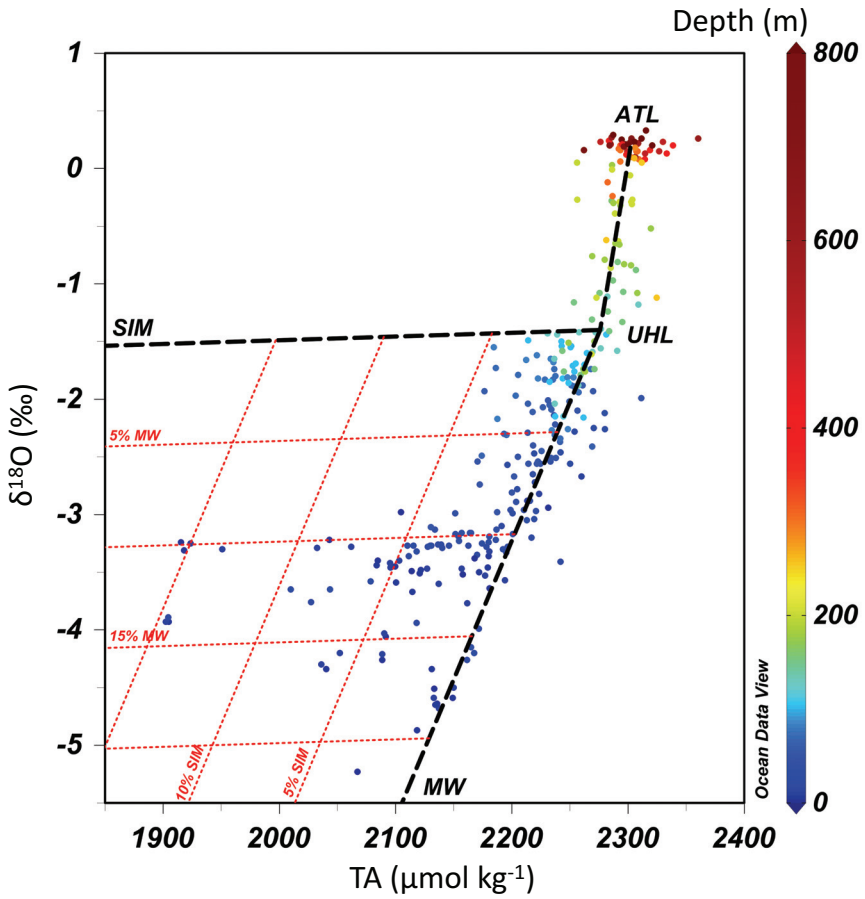

Figure 3.8: $\delta^{18}O$ versus TA of all samples, showing the water mass decomposition with end-members (MW, SIM, UHL & ATL) indicated, mixing lines (black), and colour indicating depth. Red lines indicate the fractions of MW and SIM.

Surface water composition varies greatly over the study region with large freshwater input from the Mackenzie River as well as large amounts of sea-ice melt present in the central Canada Basin (Fig. 3.9). The strong impact of the Mackenzie River is seen easily, with fractions of meteoric water greater than 20 % observed over the shelf. The impact of the river plume is seen to the east into Amundsen Gulf and travels far into the central Canada Basin with fractions of greater than 10 % in the surface in these regions. Sea-ice melt has the strongest influence in the central basin with fractions of

approximately 15 %. Substantial fractions of sea-ice melt are also seen near the shelf break at stations where meteoric water is more limited.

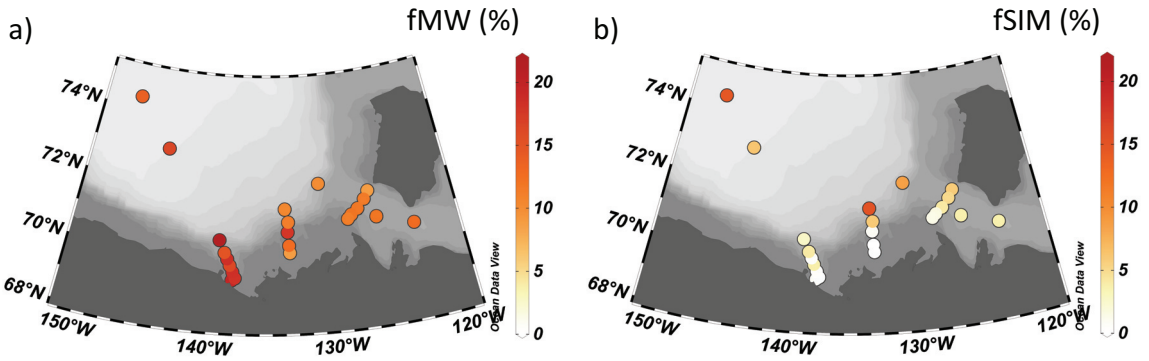

Figure 3.9: Surface values of the fraction of a) meteoric water (fMW) and b) sea-ice melt (fSIM) at all stations in the study area.

A temperature-salinity diagram for all samples is shown in Figure 3.10. Four different water masses (or mixtures of water masses) have been designated based on the water mass decomposition performed. The PML is a mixture of meteoric water, sea-ice melt and UHL water, and is characterized by low salinity and large variability in temperature. Samples designated as part of the UHL contain > 90 % UHL fraction in the water mass decomposition. Similarly, samples designated part of the ATL water mass contain > 90 % ATL fraction. The tight mixing line between UHL and ATL waters is displayed again in this T-S space. The temperature minimum of the UHL is displayed and a small temperature range is seen in waters designated UHL and UHL-ATL. The temperature maximum in the ATL layer is also displayed.

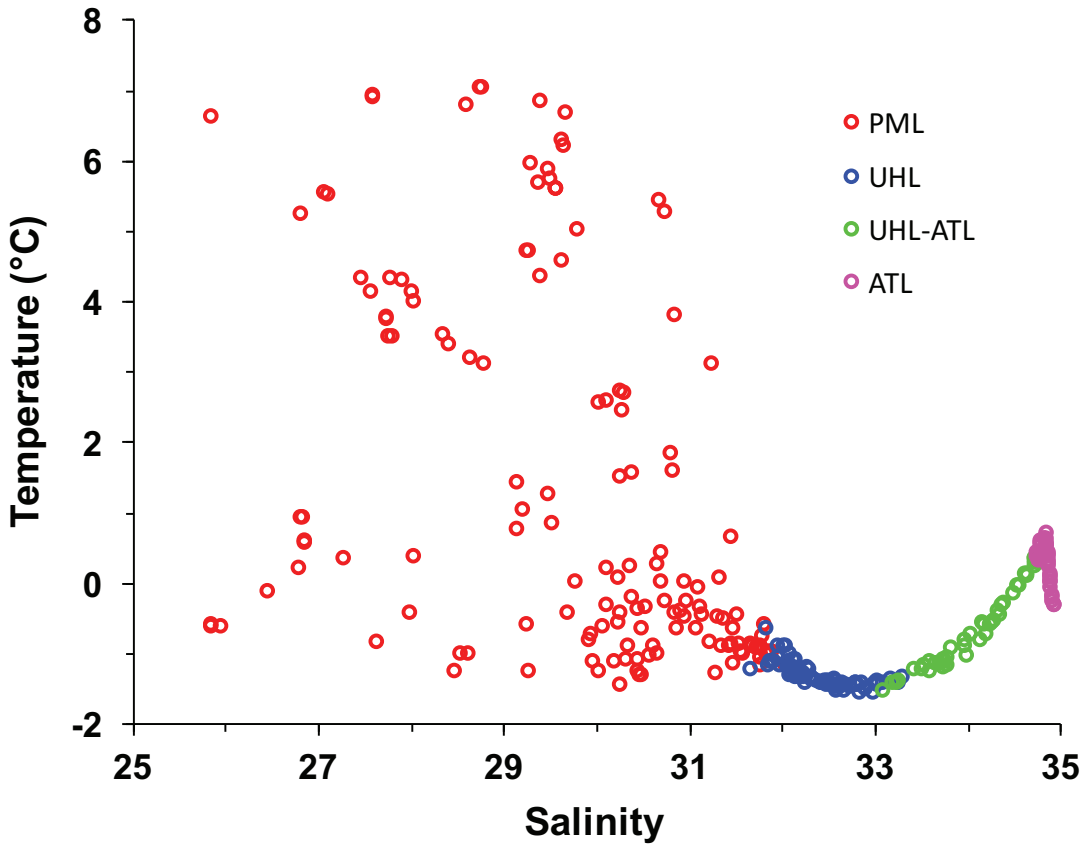

Figure 3.10: Temperature versus salinity for all samples in the study region. Colours indicate the water mass of each sample based on the water mass decomposition performed here.

The fraction of water mass types along the sampled transects on the Mackenzie Shelf and through Mackenzie Trough are shown in Figures 3.11 and 3.12 respectively. High meteoric water content is seen over the shallow shelf regions, most likely due to the influence of Mackenzie River water, and reaches into the deep basin in the surface layer. There is a large intrusion of sea ice melt coming from the deep basin towards the shelf break on the Mackenzie Shelf (Fig. 3.11b). This sea-ice may be transported south in the east side of the Beaufort Gyre and pushed onto the shelf. Sea-ice melt fraction is much more limited on the Mackenzie Trough transect, with less than 6 % fSIM in the surface layer (Fig. 3.12b). The topography of the two transects creates differences in the mid-depth influence of the UHL and the intrusion of ATL water. On the Mackenzie Shelf the

UHL dominates at mid-depth, around 100 m off the shelf, with large fractions, greater than 95 %, pushed up to shallower depths along the bottom of the shelf (Fig. 3.11c). Atlantic water is restricted to the deep layer past the shelf break; it does not intrude up onto the shallow shelf during the time in which sampling took place (Fig. 3.11d). In the Mackenzie Trough, the UHL dominates from 50 m down to approximately 200 m depth (Fig. 3.12c). The greater fraction of freshwater from the Mackenzie River restricts the influence of the UHL at the shallowest station closest to shore. Atlantic water is mostly restricted to deeper than 200 m, with a small fraction at the station furthest offshore reaching to shallower depths of approximately 150 m (Fig. 3.12d). This water mass does not intrude shallower than the 175 m isobath along the bottom of the shelf in the Trough.

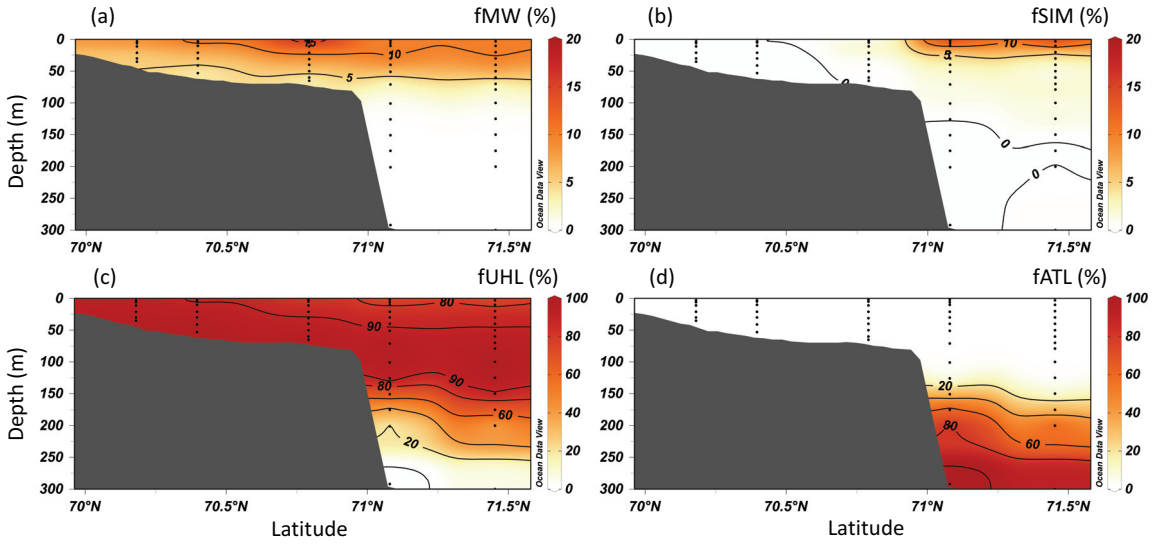

Figure 3.11: Water mass composition in the top 300 m of the Mackenzie Shelf transect. The fraction of a) MW, b) SIM, c) UHL, and d) ATL water masses. Measurements are indicated by black dots.

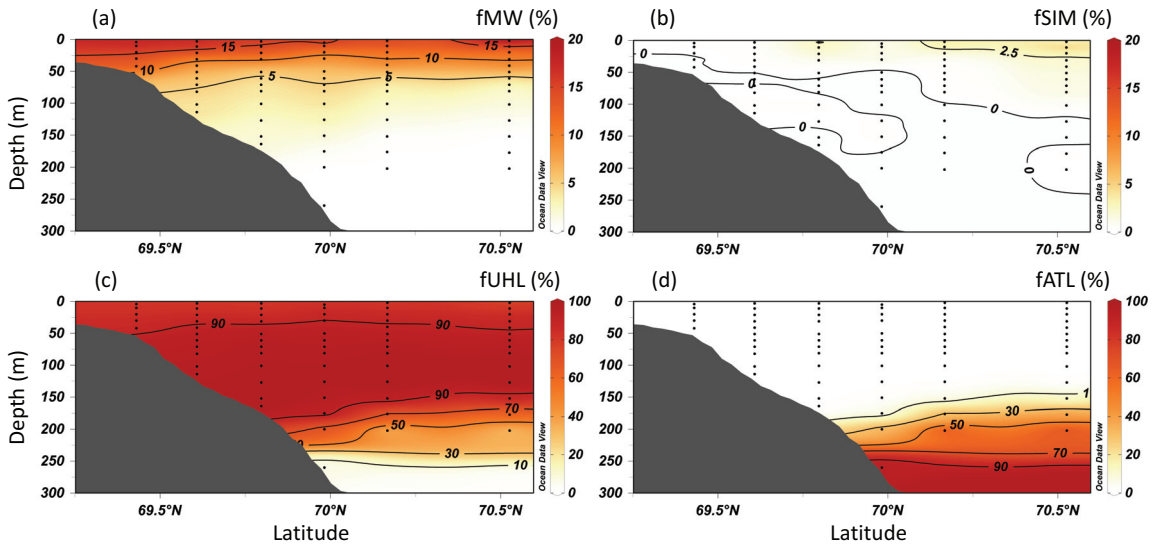

Figure 3.12: Water mass composition in the top 300 m of the Mackenzie Trough transect. The fraction of a) MW, b) SIM, c) UHL, and d) ATL water masses. Measurements are indicated by black dots.

3.4 Mackenzie Shelf Circulation

The modelled velocity in the top 10 m of the water column on the Mackenzie Shelf is shown in Figures 3.13a and b for two time periods displaying the two opposite modes of circulation found during the study period in the fall of 2014. During the period from August 16th to 20th, surface flow goes to the west along the Mackenzie Shelf. From September 5th to 9th mean surface flow is towards the east. In the middle of the shelf, cross-shelf transport of surface water is evident at both times, with off-shelf flow from August 16th to 20th and on-shelf flow from September 5th to 9th. In both cases, the topography of Cape Bathurst creates intensified surface currents in the mean direction of flow. Surface flow is also altered at the Mackenzie Trough, as topography becomes more complicated and the influence of the Mackenzie River is at its greatest. The modelled velocity at the 56 m depth horizon shows the strong influence of the shelf-break jet from both August 16th to 20th (Fig. 3.13c) going to the west and from September 5th to 9th (Fig.

3.13d) going to the east. The water flow follows the topography of the shelf quite closely in both cases. This is shown strongly at the Mackenzie Trough, but is also evident with cross-shelf movement through the middle of the sampled transect, due most likely to bathymetric changes at Kugmallit Valley, which has previously been documented as a location of enhanced cross-shelf transport (*Williams et al*., 2008). From August 16th to 20th the modelled velocity at the 92 m depth horizon shows an accelerated shelf-break jet (Fig. 3.13e). The velocity from September 5th to 9th at the 92 m depth horizon (Fig. 3.13f) shows the eastward flowing shelf-break jet at a similar magnitude of velocity as at a depth of 56 m.

These two different periods display the two opposite modes of circulation on the Mackenzie Shelf. From August 16th to 20th, the shelf-break jet is going to the west, allowing for upwelling to take place along the shelf; water in the surface layer is pushed off-shelf towards the basin and water at depth is brought onto the shelf. From September 5th to 9th, the shelf-break jet is moving to the east, creating a situation in which downwelling takes place, with water at the surface moving towards the shore, and water at depth moving out past the shelf-break. These two periods are investigated further to look at the upwelling and downwelling circulation present in the fall of 2014.

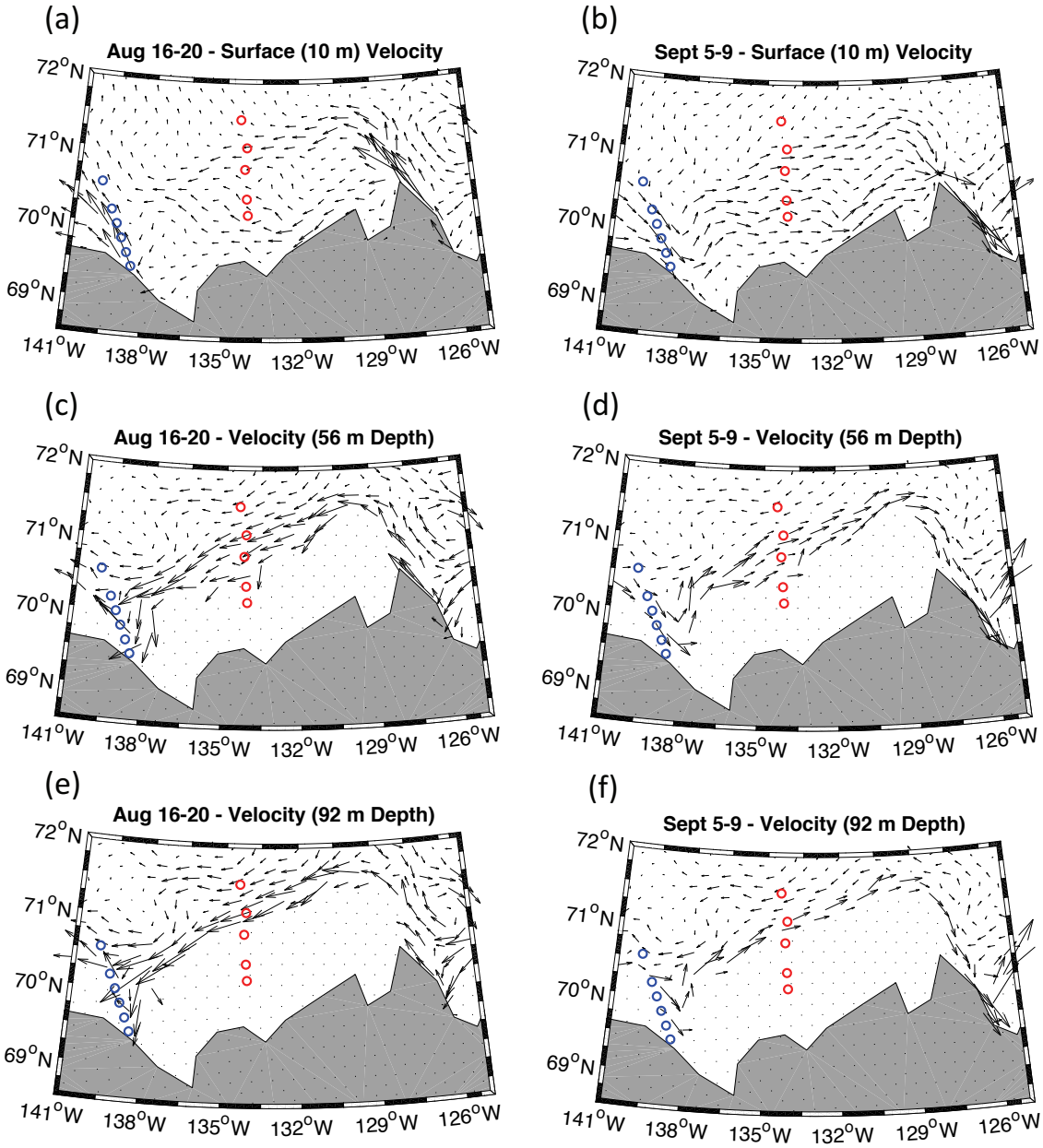

Figure 3.13: Modelled velocity in the top 10 m of the water column (a and b), at 56 m depth (c and d), and at 92 m depth (e and f) on the Mackenzie Shelf during two time periods, from August 16th to 20th (a, c and e) and from September 5th to 9th (b, d and f) in the fall of 2014. Red circles indicate the stations sampled as part of the Mackenzie Shelf transect and blue circles indicate stations sampled as part of the Mackenzie Trough transect.

3.5 Wind Forcing

Wind data was taken from the gridded reanalysis data from the Canadian Meteorological Centre (*Smith et al.*, 2014). The location selected is on the Mackenzie Shelf, near the middle of the transect, located at 70.31° N, -133.59° W. Figure 3.14 shows the wind direction and magnitude averaged every 6-hours through August and September of 2014. Oscillations between strong northerly and southerly winds are a prevailing feature. From August 6th to 16th the wind field is dominated by northeasterly winds with magnitudes of > 20 m s^{-1}. Between August 26th and September 10th periods of strong southerly winds are interrupted by short periods of strong northerly winds with maximum magnitudes of > 50 m s^{-1} in both directions. September 14th to 16th and 26th to 30th are periods of sustained southeasterly winds reaching magnitudes of up to 40 m s^{-1}.

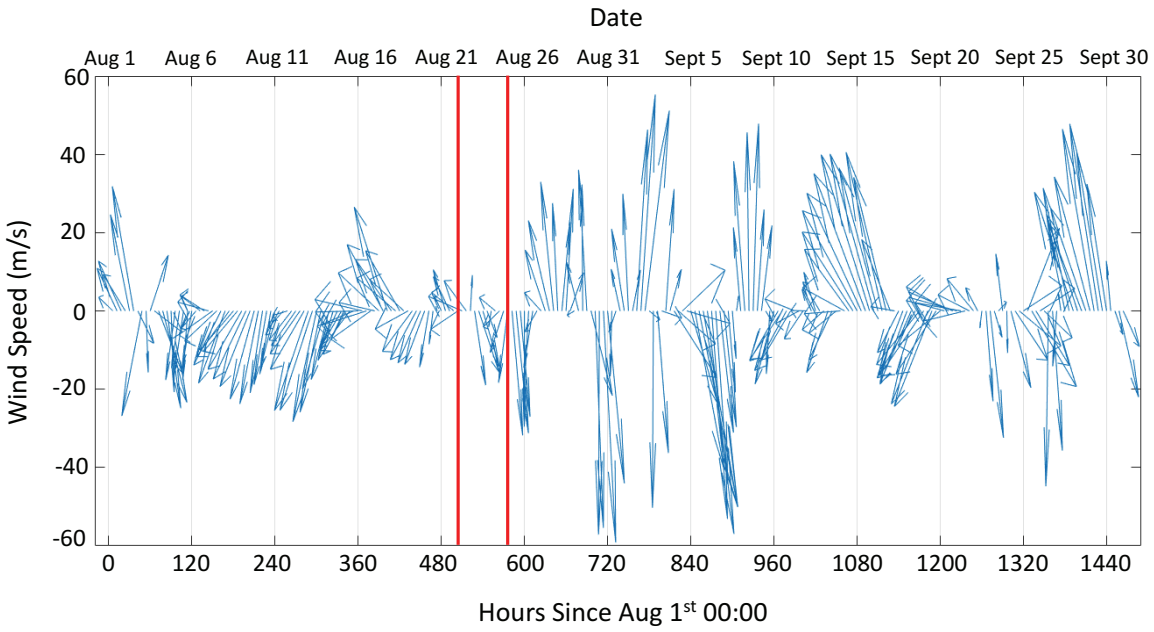

Figure 3.14: 6-hour averaged winds for August and September of 2014 on the Mackenzie Shelf (location 70.31 °N, -133.59 °W) from gridded reanalysis data from the Canadian Meteorological Centre. Red lines indicate the time period in which sampling of the Mackenzie Shelf transect took place.

Water sampling on the Mackenzie Shelf transect was done from August 22nd to 24th. There is evidence of upwelling from the physical parameters (temperature and salinity) as shown in Figure 3.6. Upwelling on the Mackenzie Shelf is associated with a reversal of the shelf-break jet due to northeasterly winds. From August 6th to 16th these strong winds are present over the shelf region. By the time sampling took place, these northeasterly winds had shifted and were no longer as dominant over the region, but the winds remained easterly through August 22nd. It seems possible from the wind and physical sampling data that upwelling took place on the Mackenzie Shelf between August 6th to around the 22nd of August.

3.6 Mackenzie Shelf Velocity Fields

The two-month average modelled velocities of the along-shore and cross-shelf flow for the Mackenzie Shelf section are shown in Figures 3.15a and b. The surface over the shelf is dominated by eastward along-shore flow. The westward flow of the Beaufort Gyre past the shelf-break is evident. The cross-shelf flow is primarily in the on-shelf direction over the shallow shelf and off-shelf past the shelf-break. Due to Ekman transport, westward flow going towards the Alaskan Shelf is associated with upwelling transport onto the shelf. This situation is seen from August 16th to 20th with strong westward along-shore transport and velocities on the shelf and in the core of the shelf-break of > 0.15 m s^{-1} (Fig. 3.15c). This westward transport throughout the water column coincides with water velocities in the cross-shelf direction indicative of upwelling (Fig. 3.15d). Surface water over the shelf reaches velocities of > 0.08 m s^{-1} in the off-shelf direction in the top 5 m and velocity remains in an off-shelf direction for much of the top 15 m of the water column. Below this surface layer, water flow over the shelf is in an on-

shelf direction, reaching velocities of > 0.10 m s^{-1} at mid-depth (~ 50 m). This upwelling flow is obvious, with water at depth being moved onto the shelf and water at the surface moving out toward the shelf-break. Flow from the west going towards Amundsen Gulf is associated with downwelling transport off the shelf, a situation seen from September 5th to 9th (Fig. 3.15e and f). Along-shore velocity over the shelf and shelf-break is high, dominated by flow in the eastward direction over the entire shelf area, reaching values of > 0.16 m s^{-1} at the surface and decreasing with depth. The intensity of the westward flow in the deep basin is decreased and pushed further beyond the shelf-break as compared to the average along-shore pattern. The strong eastward flow over the shelf and shelf-break is associated with an on-shelf transport at the surface over the shelf (> 0.09 m s^{-1}) and an off-shelf transport along the shelf bottom reaching velocities of > 0.03 m s^{-1}. This cross-shelf velocity pattern shows a downwelling loop, with water at the surface pushed towards the shore and water at depth moving out toward the shelf-break.

These modelled velocities are representative of 5-day averages for the region and thus do not show the peak velocities taking place throughout the study period. The shelf-break jet or boundary current has been measured throughout the year at various locations along the Alaskan and Canadian Beaufort shelves. For example, *Pickart et al*. (2009) reported a bottom intensified shelf-break jet flowing ~ 0.15 m s^{-1} to the east over a yearlong mean across the shelf at 152°W, similarly reported by *Nikolopoulos et al*. (2009). This is the same value as the maximum modelled velocities found in the core of the shelf-break jet through the sampled transect. The reversal of the shelf-break jet due to variations in wind forcing has been shown in numerous studies along the Beaufort Shelf (e.g. Nikolopoulos et al., 2009; Pickart et al., 2013; Dmitrenko et al., 2016). Measurements of velocity from moorings in the same region across the Mackenzie Shelf

slope, such as those analyzed by *Forest et al.* (2015) from September 2009 to August 2012, show current surges of 0.20 to 0.80 m s^{-1} with frequent oscillations in current direction. The mean velocities over this period at these moorings were 0.08 to 0.14 m s^{-1}. These mean velocities are comparable to the magnitude of velocities produced by the model here for 5-day averages. It is possible that similarly strong surges in current velocity took place throughout the study period of August and September 2014 on the Mackenzie Shelf.

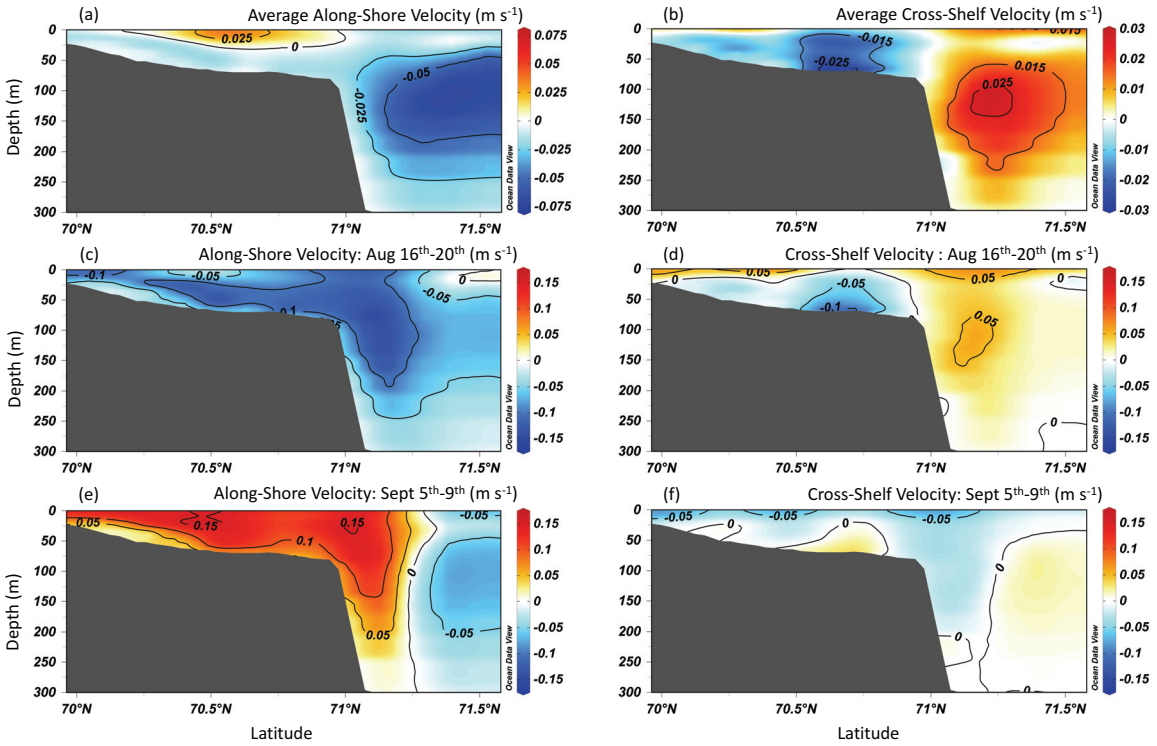

Figure 3.15: The average a) along-shore and b) cross-shelf velocity on the Mackenzie Shelf transect during August and September of 2014, the c) along-shore and d) cross-shelf velocity from August 16th to 20th 2014, and the e) along-shore and f) cross-shelf velocity from September 5th to 9th. Positive values (red) indicate eastward along-shore flow (out of the plane) and off-shelf cross-shelf flow (to the right). Negative values (blue) indicate westward along-shore flow (into the plane) and on-shelf cross-shelf flow (to the left).

3.7 Along-Shore Volume Transports

Along-shore volume transport throughout the study period along the Mackenzie Shelf transect is estimated for the top 200 m of the water column through the 120 km (in the cross-shelf direction) section (Fig. 3.16a) (section identified in Figure 2.1). This volume transport was calculated by taking the product of the depth-averaged velocity with the depth and cross-shelf area between stations. Positive values indicate eastward flow, while negative values indicate westward flow. Maximum westward transport of 0.74 Sv through the Mackenzie Shelf transect occurred from August 16th to 20th; maximum eastward transport of 0.89 Sv through the transect occurred from September 5th to 9th. For comparison, the transport of northward flowing water through the Bering Strait is approximately 1.1 Sv (*Woodgate et al.,* 2012). The along-shore volume transport through these two transects and the changes in transport direction are substantial.

In August and September of 2014, the circulation along-shore changed from a strong flow to the west to a strong flow to the east and back again (Fig. 3.16a). Correlation between along-shore wind in the northeasterly (southwesterly) direction and upwelling (downwelling) on the Mackenzie Shelf has been shown in numerous studies and models (e.g. *Carmack & Kulikov*, 1998; *Yang et al*., 2006; *Mathis et al*., 2012). In this study, the two periods of strongest upwelling on the Mackenzie Shelf, August 11th to 20th and September 15th to 24th, occur with strong (> 20 m s^{-1}) and sustained northeasterly winds at the beginning of these periods (Fig. 3.14). The period of strongest downwelling, from August 31st to September 9th, corresponds to strong southwesterly winds (> 40 m s^{-1}) at the beginning of this period, with strong wind reversals throughout.

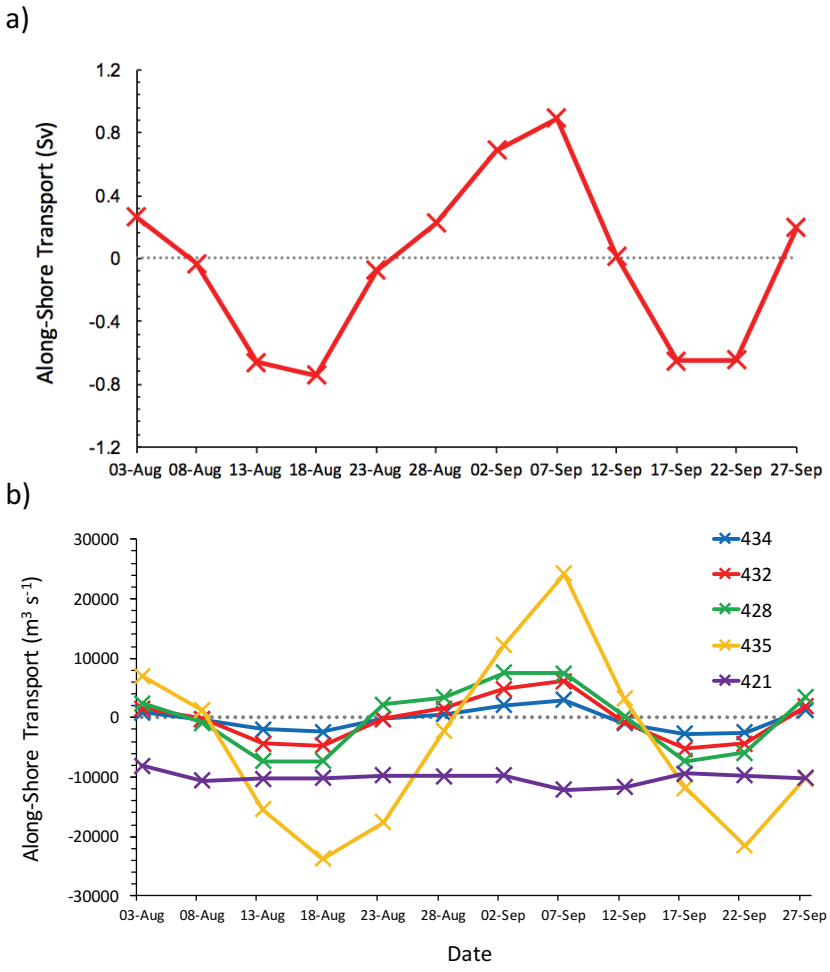

Figure 3.16: The along-shore volume transport through the Mackenzie Shelf transect for the study period of August and September 2014. A) shows the total integrated volume transport for 120 km in the cross-shelf direction. Transport at each station, with a 1 km cross-shelf distance, is shown in b). Transports are calculated from 5-day averages of modelled velocity.

The oscillating along-shore volume transport is dominated by changes over the slope. This is evident if the transport is calculated at the specific sampled station locations. Along-shore volume transports for the stations on the transect are calculated through the water column, to a maximum depth of 200 m, by taking the sum of the products of the along-shore velocity and a cross-shelf distance of 1 km (Fig. 3.16b). Bottom depth is taken from the shipboard depth sounder when sampling took place. All three stations on the shelf (434, 432 and 428) show the same oscillating change in along-

shore transport. Station 435, on the slope, dominates the along-shore volume transport as it is located at the position of the shelf-break jet. Station 421, located beyond the slope in the deep basin, shows a negative total along-shore transport throughout the study period. This station is under the influence of the Beaufort Gyre, which is consistently flowing in a westward direction at this location. During the 2-month study period there is an oscillation between two dominate flow patterns represented by positive and negative total transport in the along-shore direction.

3.8 Cross-Shelf Carbon Transport

Cross-shelf flux calculations were done for the Mackenzie Shelf transect to investigate the exchange of inorganic carbon and alkalinity between the shelf and the deep basin during an upwelling period. Fluxes were calculated by taking the product of linearly gridded DIC or TA measurements and cross-shelf velocity values from the ANHA4 simulation through the water column. The DIC flux (mol C d^{-1} m^{-2}) at the shelf and slope stations for the period of the largest on-shelf flux, from August 16th to 20th, are shown in Figure 3.17. During this period of greatest westward along-shore transport, the cross-shelf DIC flux is off-shore at all stations in the top 10 to 25 m of the water column, reaching values of 16.7 x 10^3 mol C d^{-1} m^{-2} (TA flux: 18.1 x 10^3 mol C d^{-1} m^{-2}) at station 432. At the shelf stations (434, 432 and 428) the DIC flux is on-shelf below the surface layer. Stations 434 and 432 have maximum on-shelf fluxes of 6.6 x 10^3 (TA flux: 6.8 x 10^3) and 3.7 x 10^3 mol C d^{-1} m^{-2} (TA flux: 3.8 x 10^3 mol C d^{-1} m^{-2}) respectively at mid-depth. At station 428, on-shelf fluxes reach values of 16.9 x 10^3 mol C d^{-1} m^{-2} (TA flux: 17.4 x 10^3 mol C d^{-1} m^{-2}) near the bottom of the water column. This on-shelf flux near the

ocean floor transports water sourced from the UHL, bringing water high in remineralization products and DIC onto the shelf.

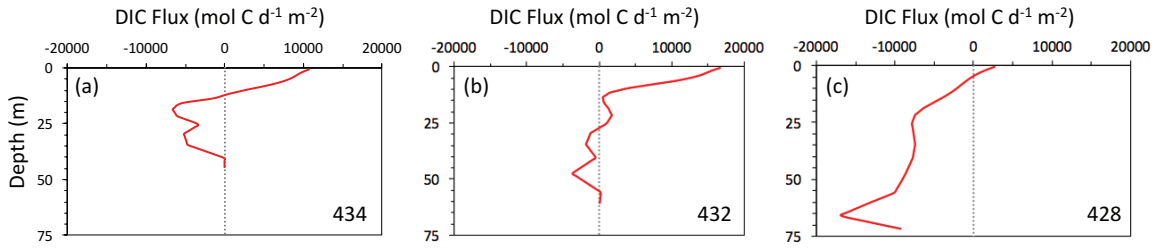

Figure 3.17: Cross-shelf fluxes of DIC (mol C d^{-1} m^{-2}) at stations a) 434, b) 432 and c) 428 on the Mackenzie Shelf. Positive values indicate off-shelf fluxes while negative values indicate on-shelf fluxes.

The amount of metabolic DIC that is brought onto the shelf and the extent to which it alters the pCO_2 and pH conditions depends on the amount of water transported and the source water composition. The ratio of DIC:TA in the water being moved along the bottom of the shelf is a parameter giving insight into the carbonate system properties of the water mass. At stations 434, 432 and 428 on the shelf, the DIC:TA ratio changes significantly with depth. Water being upwelled from August 16th to 20th (Fig. 3.17, negative DIC flux) reveals DIC:TA ratios of greater than 0.975 at all three stations. This is higher than the ratio in surface waters moved out towards the deep basin (August 16th to 20th), which have ratios ranging from 0.92 to 0.94. This greater DIC:TA ratio means that there is a greater amount of metabolic DIC in the water being upwelled, contributing to increased pCO_2 and decreased pH and Ω_{Ar} levels. Water in the surface layer has a lower ratio of DIC:TA, creating the potential for an increased uptake of CO_2 from the atmosphere. The influence of air-sea exchange of CO_2 is not analyzed in detail here. It is assumed that any air-sea exchange would be a small fraction of lateral exchange on these

timescales of days to weeks. During the time of measurement, surface pCO_2 levels along the Mackenzie Shelf transect were quite low, ranging from 278 to 339 μatm. If there was uptake of CO_2 by the surface ocean, this would serve to increase the magnitude of the DIC flux in the surface layer.

Cross-shelf mass transport of carbon was calculated for the three stations on the shelf (434, 432 and 428) for the period of August 16th to 20th (Table 3.1). These transports are integrated through the water column with a 10 km along-shore distance to include the area of the shelf that is under similar influence of water movement, considering the bathymetric changes as part of Kugmallit Valley (*Williams et al.,* 2008). From August 16th to 20th, when the along-shore flow is westward, the cross-shelf transport indicates an upwelling flow over the shelf. In the top 10 m at all three stations the transport is off-shelf, ranging from $0.1 \pm 1 \times 10^{-3}$ to $14 \pm 3 \times 10^{-3}$ Tg C d^{-1}. Below the surface layer, the cross-shelf transport is on-shelf at all three stations, with maximum transport at station 428 of $65 \pm 15 \times 10^{-3}$ Tg C d^{-1}.

Table 3.1. Cross-shelf mass transports (Tg C d^{-1}) calculated from measurements of DIC on the Mackenzie Shelf transect for the three shelf stations. The integrated mass transport is shown for both the top 10 m at each station and the full-water column below the top 10 m with an along-shore distance of 10 km. Positive values indicate off-shelf transport; negative values indicate on-shelf transport.

Station	Water Column Section	Cross-Shelf Mass Transport (Tg C d^{-1})
434	Top 10 m	$9 \pm 2 \times 10^{-3}$
	10 – 45 m	$-14 \pm 3 \times 10^{-3}$
432	Top 10 m	$14 \pm 3 \times 10^{-3}$
	10 – 61 m	$-3 \pm 3 \times 10^{-3}$
428	Top 10 m	$0.1 \pm 1 \times 10^{-3}$
	10 – 72 m	$-65 \pm 15 \times 10^{-3}$

There are two periods throughout August and September of 2014 lasting > 10 days in which the cross-shelf transport brings water from the basin onto the Mackenzie Shelf. During these episodes, water from the UHL high in DIC and other remineralization products is brought onto the shelf and possibly to the surface over the Mackenzie Shelf. The period of off-shelf transport lasts for ~ 15 days in the region, offsetting the on-shelf flux of these waters and carrying remineralization products back to the deep basin. Nevertheless, the average transport through the two months carries water onto the shelf. This long-term upwelling activity has consequences for ocean acidification on the shelf in the bottom waters as well as air-sea exchange of CO_2 and the sink or source status of the shelf, discussed further in Section 3.10. Surface water high in meteoric water content is also delivered beyond the shelf-break into the Beaufort Gyre as upwelling takes place.

3.9 Impacts of Upwelling on Carbonate Chemistry

Evidence of upwelling activity on the shelf is identified in the gradients of DIC, TA and δ^{13}C-DIC across the shelf (Fig. 3.18a-d). The on-shore transport of all three parameters from deeper water is evident when comparing the values at the 50 m depth horizon across the three stations. The values of the onshore gradients for DIC and TA are -2.06 μmol m^{-3} m^{-1} and -0.91 μmol m^{-3} m^{-1} respectively. The DIC:TA ratio of these gradients is 2.26, meaning that more DIC is brought onto the shelf relative to TA. This is important because a higher ratio of DIC:TA means an increased pCO_2 content of the water as well as a decrease in the pH and the saturation states of carbonate minerals. If these waters are brought to the surface via upwelling or vertical mixing, the net flux of CO_2 over the shelf region may be altered. Outgassing may occur, releasing CO_2 to the atmosphere, or the uptake of CO_2 by the surface ocean may be suppressed. In this case,

the surface water measurements of pCO_2 were low when sampling took place. The gradient of δ^{13}C-DIC across the shelf is positive (Fig. 3.18d), opposite to that of DIC and TA. It reaches lowest values along the shelf bottom, showing the signature of UHL source water and an excess remineralization of organic matter at depth on the shelf.

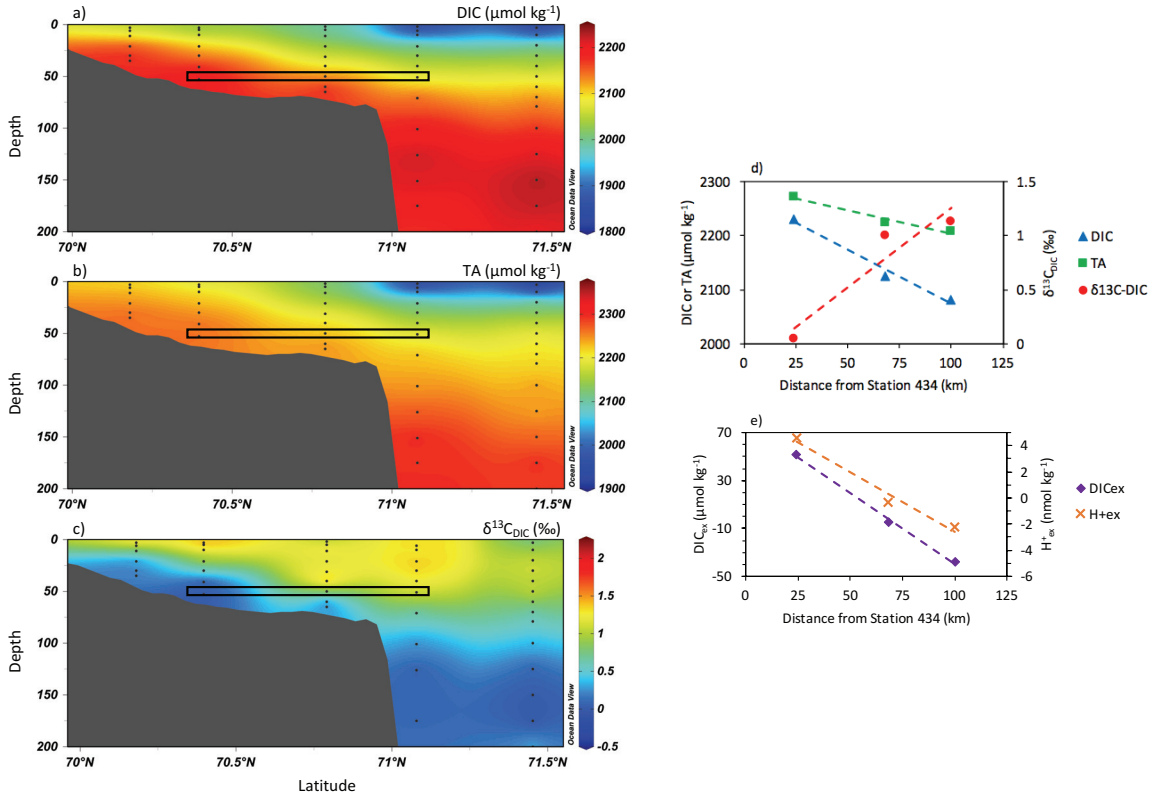

Figure 3.18: Distributions of a) DIC, b) TA and c) δ^{13}C-DIC on the Mackenzie Shelf transect. Black boxes indicate depth of 50 m at stations 432, 428 and 435, going outward from the shelf. Measurements are indicated by black dots. Chemical gradients at the 50 m depth horizon along the transect are shown in d) and e).

To investigate the delivery of DIC to the shallow shelf, the effects on the source or sink status of the shelf, and the pH conditions, the excess DIC (DIC_{ex}) and excess protons (H^+_{ex}) were calculated relative to the equilibrated surface conditions (following the methods of *Burt et al.,* 2013). The surface pCO_2 was assumed to be 400 µatm in equilibrium with the atmosphere. DIC_{ex} and H^+_{ex} were then calculated as the difference

between the observed values at 50 m depth and those occurring with the same TA, temperature and salinity conditions with pCO_2 values of 400 µatm:

$$DIC_{ex} = DIC_{obs} - DIC_{(pCO_2=400)} \quad (3.1)$$

$$H^+_{ex} = H^+_{obs} - H^+_{(pCO_2=400)} \quad (3.2)$$

The value of the gradient in DIC_{ex} across the shelf is -1.19 µmol kg^{-1} km^{-1} and the value of the gradient in H^+_{ex} is -0.09 nmol kg^{-1} km^{-1} (Fig. 3.18e). Both quantities display negative gradients, with positive values closer to shore along the shelf bottom at station 432. DIC_{ex} reaches a value of 51.4 µmol kg^{-1} and H^+_{ex} reaches a value of 4.57 nmol kg^{-1} meaning that there is excess DIC and H^+ in this water relative to the equilibrated surface conditions. If this water from the shelf is upwelled, the surface water pCO_2 and pH conditions will be altered, lowering the pH and raising the pCO_2 at the surface and creating the possibility for outgassing or a decrease in uptake of CO_2. This high pCO_2, low pH water along the bottom of the shelf is seen in Figures 3.3e and h.

3.10 Ocean Acidification & Freshwater Impact

Ocean acidification in the Arctic is complicated by several different changing parameters including warming, sea-ice loss, surface freshening and changes in primary production (*Carmack et al.*, 2016). During sampling, a layer of high pCO_2, low pH water resides at depth on the shelf (Fig. 3.3e and h). This could in part be due to high primary production in the euphotic zone and subsequent remineralization at depth (*Bates et al.*, 2013), but also due to the upwelling of water from beyond the shelf-break onto the shelf, as seen in this study. This bottom layer is sourced from the UHL where a DIC maximum

consistently resides (*Anderson et al.*, 2010; *Yamamoto-Kawai et al.*, 2013). The UHL source water is of Pacific-origin, and is preconditioned before entering the Arctic to have low Ω_{Ar} values (*Shadwick et al.*, 2013; *Yamamoto-Kawai et al.*, 2013). This water is seen in Figure 3.19, centred at a salinity of 33.1 and a temperature minimum, having pCO_2 values over 600 µatm and showing undersaturation of aragonite ($\Omega_{Ar} < 1.0$). In this case, the undersaturated water mass is not at the surface over the shelf, but sustained periods of upwelling could bring this high pCO_2 water to the surface and create outgassing of CO_2 (e.g. *Mathis et al.*, 2012).

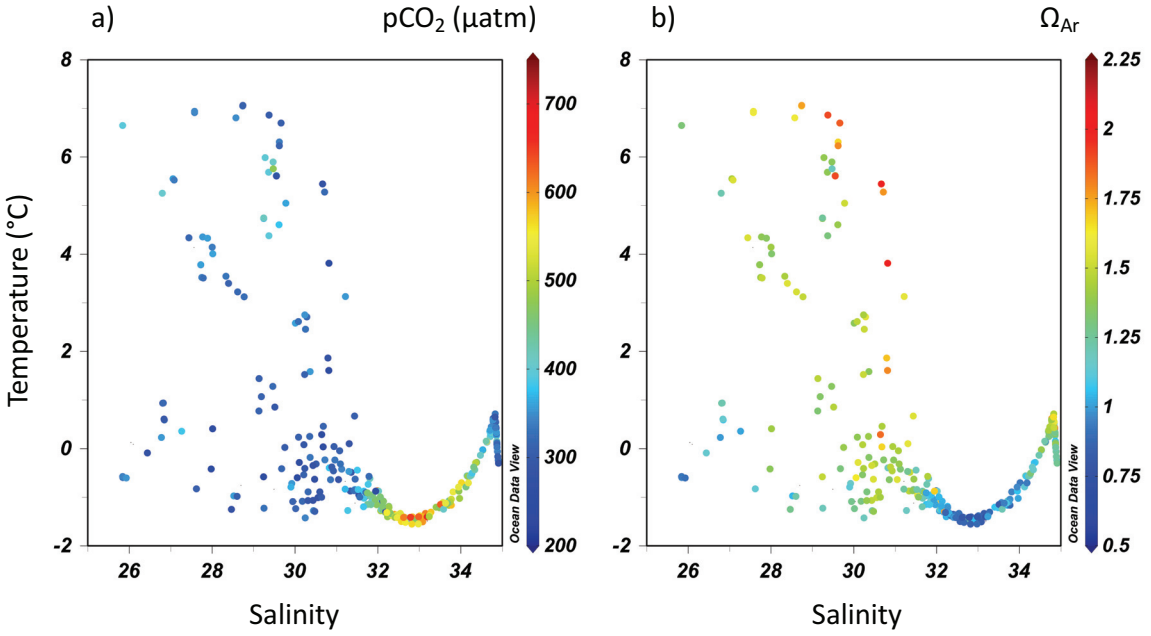

Figure 3.19: Temperature versus salinity for all samples in the study region. Colours showing a) values for pCO_2 and b) Ω_{Ar}.

Surface waters with low salinity and low temperature show decreased saturation states and even undersaturation of aragonite, particularly in areas with a large fraction of sea-ice melt such as the Canada Basin. The input of sea-ice melt with low values of DIC, TA and $[Ca^{2+}]$ dilutes the chemical constituents in the surface water, resulting in low

values of Ω_{Ar} (*Yamamoto-Kawai et al*., 2011). Less ice cover also results in increased air-sea gas exchange, potentially adding more CO_2 to the surface ocean in these areas of high ice melt with low pCO_2 values (*Mucci et al*., 2010). Input of water from the Mackenzie River does not decrease the saturation of aragonite as much as sea-ice melt because it contains higher TA values and a lower ratio of DIC:TA, and allows for an increased uptake of atmospheric CO_2. Surface flow at the Mackenzie Shelf transect is on average off-shelf during the study period, carrying freshwater out into the surface layer of the Canada Basin. Upwelling of water onto the Mackenzie Shelf due to northeasterly winds pushes the river plume offshore (*Williams and Carmack*, 2015). Stations in the middle of the Canada Basin show a high content of meteoric water in the surface (13-17 %), adding to the stratification of the Beaufort Gyre. Increased stratification produces a stronger and shallower halocline and in turn allows for higher temperatures, prevents the transport of CO_2 to the deep ocean, restricts CO_2 to the shelf bottom where pH and Ω are decreased, and suppresses the supply of nutrients leading to a decrease in primary production (*Carmack et al*., 2016). Increasing freshwater content of the Beaufort Gyre is forced by anticyclonic winds (*Stewart and Haine,* 2013) and has been observed to increase in recent years due to sea-ice melt, the transport of river water due to upwelling (*Pickart et al*., 2013) and an increased inflow of fresh Pacific Water (*Woodgate et al.,* 2012). This freshwater accumulation may have far-reaching effects on deep-water formation in the North Atlantic (*Aagaard et al*., 1985) if wind conditions are altered over the Beaufort Gyre.

3.11 Future Projections: Fall to the Rest of the Year

The effects of large atmospheric circulation processes and local winds have been shown to greatly affect the direction of along-shore transport of water and the resulting cross-shelf transport of DIC and remineralization products on the Mackenzie Shelf. Strengthening of the Beaufort High and a greater frequency of Aleutian Low storms will lead to an enhancement of easterly winds, promoting upwelling fluxes and offshore surface transport (*Mathis et al*., 2012). Increased easterly winds would export a greater volume of ice from the Beaufort Gyre, allowing greater solar radiation to increase surface layer hear content (*Wood et al*., 2013), as well as reduce the transport of Pacific Summer Water in the shelf-break jet, meaning more mass and heat would be transported out into the Canada Basin instead of being diverted to the east along the shelf-break (*Brugler et al*., 2014).

In the future, ice edge retreat away from the shore is predicted to start earlier and encompass a greater area of open water (*Barber et al*., 2015). This temporal and spatial increase in open water over shelf regions provides a potential for more upwelling leading to greater nutrient delivery (*Williams & Carmack*, 2015) and denser water on the shelf, pre-conditioning for brine formation to occur at freeze-up (*Backhaus et al*., 1997). In contrast to this, in the ice-covered months, if flaw leads remain open for longer, upwelling winds can continue to stress the surface and restrict dense water movement off-shelf (*Williams et al*., 2008). Thinning and reduced sea-ice cover will lead to less internal stress of the ice pack (*Shimada et al*., 2006), creating a greater response to upwelling favourable wind-stress (*Williams and Carmack,* 2015). The delivery of UHL water with greater DIC content to the continental shelves of the Beaufort Sea due to upwelling will

have strong effects on the carbonate system and the pCO_2 of both surface and deep waters on the shelf.

CHAPTER 4: CONCLUSION

Carbonate system parameters were measured in the Beaufort Sea during August and September of 2014. The cross-shelf transport of inorganic carbon during upwelling circulation was found using the velocity fields from output of the ANHA4 simulation. The upwelling of water from the UHL onto the shelf alters the carbonate system and poses a potential threat to calcifying organisms. Upwelling of this water to the surface potentially changes the net flux of CO_2 over the shelf, with possible outgassing of CO_2 or a suppression of the uptake of CO_2. The mean circulation through the two months showed upwelling to be the dominant process, but it is important to look at how representative these two months are of other years, and of other times of the year as well. Future monitoring should concentrate on more continuous sampling to catch the system in different modes of upwelling or downwelling. This would provide a better picture of where nutrients, DIC, and remineralization products are cycled with these strong current reversals. Models like the ANHA4 simulation utilized here can be used to look further into when upwelling will occur on the shelf and how much carbon cycling will be altered by these events. Combining these results with other datasets such as moorings and in-situ measurement platforms could be beneficial for understanding carbon budgets in these traditionally hard to reach areas.

BIBLIOGRAPHY

Aagaard K., J. H. Swift, and E. C. Carmack, Thermohaline circulation in the Arctic Mediterranean Seas, *Journal of Geophysical Research: Oceans, 90,* 4833-4846, doi:10.1029/JC090iC03p04833, 1985.

Aagaard, K., A synthesis of the Arctic Ocean circulation, *Rapports et Proces-verbaux des Réunions. Conseil International pour l'Exploration de la Mer, 188*, 11-22, 1989.

Aagaard K., and E. C. Carmack, The role of sea ice and other fresh water in the Arctic circulation, *Journal of Geophysical Research: Oceans, 94*, 14485-14498, doi:10.1029/JC094iC10p14485, 1989.

Anderson, L. G., and R. W. Macdonald, Observing the Arctic Ocean carbon cycle in a changing environment, *Polar Research, 34*, 26891, doi:10.3402/polar.v34.26891, 2015.

Anderson, L. G., T. Tanhua, G. Björk, S. Hjalmarsson, E. P. Jones, S. Jutterström, B. Rudels, J. H. Swift, and I. Wåhlstöm, Arctic ocean shelf-basin interaction: An active continental shelf CO_2 pump and its impact on the degree of calcium carbonate solubility, *Deep-Sea Research I, 57*, 869-879, 2010.

Backhaus, J. O., H. Fohrmann, J. Kämpf, and A. Rubino, Formation and export of water masses produced in Arctic shelf polynyas – process studies of oceanic convection. *ICES Journal of Marine Science, 54*, 366-382, 1997.

Bamber, J., M. van den Broeke, J. Ettema, J. Lenaerts, and E. Rignot, Recent large increases in freshwater fluxes from Greenland into the North Atlantic, *Geophysical Research Letters, 39*, L19501, doi:10.1029/2012GL052552, 2012.

Barber, D. G., and J. M. Hanesiak, Meteorological forcing of sea ice concentrations in the southern Beaufort Sea over the period 1979 to 2000, *Journal of Geophysical Research, 109*, C06014, doi:10.1029/2003JC002027, 2004.

Barber, D. G., H. Hop, C. J. Mundy, B. Else, I. A. Dmitrenko, J.-É. Tremblay, J. K. Ehn, P. Assmy, M. Daase, L. M. Candlish, and S. Rysgaard, Selected physical, biological and biogeochemical implications of a rapidly changing Arctic Marginal Ice Zone, *Progress in Oceanography, 139*, 122-150, 2015.

Bates, N. R., Air-sea CO_2 fluxes and the continental shelf pump of carbon in the Chukchi Sea adjacent to the Arctic Ocean, *Journal of Geophysical Research, 111*, C10013, doi:10.1029/2005JC003083, 2006.

Bates, N. R., M. I. Orchowska, R. Garley, and J. T. Mathis, Summertime calcium carbonate undersaturation in shelf waters of the western Arctic Ocean – how biological processes exacerbate the impact of ocean acidification, *Biogeosciences, 10*, 5281-5309, 2013.

Borges, A. V., Do we have enough pieces of the jigsaw to integrate CO2 fluxes in the coastal ocean? *Estuaries, 28*, 3-27, 2005.

Broecker, W. S., T. Takahashi, H. J. Simpson, and T.-H. Peng, Fate of fossil fuel carbon dioxide and the global carbon budget, *Science, 206*, 409-418, 1979.

Brown, K. A., F. McLaughlin, P. D. Tortell, M. Yamamoto-Kawai, and R. Francois, Sources of dissolved inorganic carbon to the Canada Basin halocline: A multitracer study, *Journal of Geophysical Research: Oceans, 121*, 2918-2936, doi:10.1002/2015JC011535, 2016.

Brugler, E. T., R. S. Pickart, G. W. K. Moore, S. Roberts, T. J. Weingartner, and H. Statscewich, Seasonal to interannual variability of the Pacific water boundary current in the Beaufort Sea, *Progress in Oceanography, 127*, 1-20, 2014.

Burt, W. J., H. Thomas, and J.-P. Auclair, Short-lived radium isotopes on the Scotian Shelf: Unique distribution and tracers of cross-shelf CO_2 and nutrient transport, *Marine Chemistry, 156*, 120-129, 2013.

Carmack, E. C., and E. A. Kulikov, Wind-forced upwelling and internal Kelvin wave generation in Mackenzie Canyon, Beaufort Sea, *Journal of Geophysical Research: Oceans, 103*, 18447-18458, doi:10.1029/98JC00113, 1998.

Carmack, E. C., and R. W. Macdonald, Oceanography of the Canadian Shelf of the Beaufort Sea: A setting for marine life, *Arctic, 55*, 29-45, 2002.

Carmack, E., and D. C. Chapman, Wind-driven shelf/basin exchange on an Arctic shelf: The joint roles of ice cover extent and shelf-break bathymetry, *Geophysical Research Letters, 30*, OCE 9, doi:10.1029/2003GL017526, 2003.

Carmack, E., and P. Wassmann, Food webs and physical-biological coupling on pan-Arctic shelves: Unifying concepts and comprehensive perspectives, *Progress in Oceanography, 71*, 446-477, 2006.

Carmack, E. C., R. W. Macdonald, and J. E. Papadakis, Water mass structure and boundaries in the Mackenzie shelf estuary, *Journal of Geophysical Research: Oceans, 94*, 18043-18055, doi:10.1029/JC094iC12p18043, 1989.

Carmack, E. C., M. Yamamoto-Kawai, T. W. N. Haine, S. Bacon, B. A. Bluhm, C. Lique, H. Melling, I. V. Polyakov, F. Straneo, M.-L. Timmermans, and W. J. Williams, Freshwater and its role in the Arctic Marine System: Sources, disposition, storage, export, and physical and biogeochemical consequences in the Arctic and global oceans, *Journal of Geophysical Research: Biogeosciences, 121*, 675-717, doi:10.1002/2015JG003140, 2016.

Ciais, P., C. Sabine, G. Bala, L. Bopp, V. Brovkin, J. Canadell, A. Chhabra, R. DeFries, J. Galloway, M. Heimann, C. Jones, C. Le Quere, R. B. Myneni, S. Piao, and P. Thornton, Carbon and Other Biogeochemical Cycles, in: *Climate Change 2013: The Physical Science Basis. Contributions of Working Group I to the Fifth Assessment Report of the Intergovernmental Panel on Climate Change*, Cambridge University Press, Cambridge, United Kingdom and New York, NY, USA, 2013.

Cohen, J., J. A. Screen, J. C. Furtado, M. Barlow, D. Whittleston, D. Coumou, J. Francis, K. Dethloff, D. Entekhabi, J. Overland, and J. Jones, Recent Arctic amplification and extreme mid-latitude weather, *Nature Geoscience, 7*, doi:10.1038/NGEO2234, 2014.

Cooper, L. W., J. W. McClelland, R. M. Holmes, P. A. Raymond, J. J. Gibson, C. K. Guay, and B. J. Peterson, Flow-weighted values of runoff tracers ($\delta^{18}O$, DOC, Ba, alkalinity) from the six largest Arctic rivers, *Geophysical Research Letters, 35*, L18606, doi:10.1029/2008GL035007, 2008.

Dai, A., T. Qian, K. E. Trenberth, and J. D. Milliman, Changes in continental freshwater discharge from 1948 to 2004, *Journal of Climate, 22*, 2773–2792, 2009.

Dickson, A. G., An exact definition of total alkalinity and a procedure for the estimation of alkalinity and total inorganic carbon from titration data, *Deep Sea Research Part A, Oceanographic Research Papers, 328*, 609-623, 1981.

Dickson, A. G., and F. J. Millero, A comparison of the equilibrium constants for the dissociation of carbonic acid in seawater media, *Deep Sea Research Part A, Oceanographic Research Papers, 34*, 1733-1743, doi:10.1016/0198-0149(87)90021-5, 1987.

Dickson, A. G., C. L. Sabine, and J. R. Christian, *Guide to best practices for ocean CO_2 measurements*, PICES Special Publication 3, 2007.

Dijkstra, H. A., Arctic Ocean Circulation, in: *Dynamical Oceanography*, Springer-Verlag Berlin Heidelberg, 2008.

Dittmar, T., and G. Kattner, The biogeochemistry of the river and shelf ecosystem of the Arctic Ocean: a review, *Marine Chemistry, 83*, 103-120, 2003.

Dmitrenko, I. A., S. A. Kirillov, A. Forest, Y. Gratton, D. L. Volkov, W. J. Williams, J. V. Lukovich, C. Belanger, and D. G. Barber, Shelfbreak current over the Canadian Beaufort Sea continental slope: Wind-driven events in January 2005, *Journal of Geophysical Research: Oceans, 121*, 2447-2468, doi:10.1002/2015JC011514, 2016.

Doxaran, D., E. Devred, and M. Babin, A 50% increase in the mass of terrestrial particles delivered by the Mackenzie River into the Beaufort Sea (Canadian Arctic Ocean) over the last 10 years, *Biogeosciences, 12*, 3551-3565, 2015.

Else, B. G. T., T. N. Papakyriakou, M. G. Asplin, D. G. Barber, R. J. Galley, L. A. Miller, and A. Mucci, Annual cycle of air-sea CO_2 exchange in an Arctic Polynya Region, *Global Biogeochemical Cycles, 27*, 388-398, 2013.

Fabry, V. J., B. A. Seibel, R. A. Feely, and J. C. Orr, Impacts of ocean acidification on marine fauna and ecosystem processes, *ICES Journal of Marine Science, 65*, 414-432, 2008.

Fichefet, T., and M. Maqueda, Sensitivity of a global sea ice model to the treatment of ice thermodynamics and dynamics. *Journal of Geophysical Research: Oceans, 102*, 12609-12646, 1997.

Fofonoff, N. P., and R. C. Millard Jr., Algorithms for computation of fundamental properties of seawater, *UNESCO Technical Papers in Marine Science, 44*, 1-53, 1983.

Forest, A., M. Sampei, H. Hattori, R. Makabe, H. Sasaki, M. Fukuchi, P. Wassmann, and L. Fortier, Particulate organic carbon fluxes on the slope of the Mackenzie Shelf (Beaufort Sea): Physical and biological forcing of shelf-basin exchanges, *Journal of Marine Systems, 68*, 39-54, 2007.

Forest, A., P. D. Osborne, L. Fortier, M. Sampei, and M. G. Lowings, Physical forcings and intense shelf-slope fluxes of particulate matter in the halocline waters of the Canadian Beaufort Sea during winter, *Continental Shelf Research, 101*, 1-21, 2015.

Gattuso, J.P., M, Frankignoulle, and R. Wollast, Carbon and carbonate metabolism in coastal aquatic systems, *Annual Review of Ecology and Systematics, 29*, 405-434, 1998.

Jones, E. P., and L. G. Anderson, On the origin of the chemical properties of the Arctic Ocean halocline, *Journal of Geophysical Research: Oceans, 91*, 10759-10767, doi:10.1029/JC091iC09p10759, 1986.

Jones, E. P., L. G. Anderson, and J. H. Swift, Distribution of Atlantic and Pacific waters in the upper Arctic Ocean: Implications for circulation, *Geophysical Research Letters, 25*, 765-768, 1998.

Keeling, C. D., R. B. Bacastow, A. E. Bainbridge, C. A. Ekdahl, P. R. Guenther, and L. S. Waterman, Atmospheric carbon dioxide variations at Mauna Loa Observatory, Hawaii, *Tellus, 28*, 538-551, 1976.

King, A.W., L. Dilling, G.P. Zimmerman, D.M. Fairman, R.A. Houghton, G. Marland, A.Z. Rose, and T.J. Wilbanks, What Is the Carbon Cycle and Why Care? in: *The First State of the Carbon Cycle Report (SOCCR): The North American Carbon Budget and Implications for the Global Carbon Cycle*, National Oceanic and Atmospheric Administration, National Climatic Data Center, Asheville, NC, USA, 15-20, 2007.

Lansard, B., A. Mucci, L. A. Miller, R. W. Macdonald, and Y. Gratton, Seasonal variability of water mass distribution in the southeastern Beaufort Sea determined by total alkalinity and $\delta^{18}O$, *Journal of Geophysical Research: Oceans, 117*, C03003, doi:10.1029/2011JC007299, 2012.

Lewis, E., and D. W. R. Wallace, Program developed for CO_2 systems calculations, *ORNL/CDIAC 105*, Carbon Dioxide Information Analysis Center, Oak Ridge National Laboratory US Department of Energy, Oak Ridge, Tennessee, 1998.

Macdonald, R. W., S. M. Solomon, R. E. Cranston, H. E. Welch, M. B. Yunker, and C. Gobeil, A sediment and organic carbon budget for the Canadian Beaufort Shelf, *Marine Geology, 144*, 255-273, 1998.

MacGilchrist, G. A., A. C. Naveira Garabato, T. Tsubouchi, S. Bacon, S. Torres-Valdés, and K. Azetsu-Scott, The Arctic Ocean carbon sink, *Deep Sea Research I, 86*, 39-55, 2014.

Madec, G., NEMO ocean engine. Note du Pôle de modélisation, Institut Pierre-Simon Laplace (IPSL), France, No 27 ISSN No 1288-1619, 2008.

Masina, S., A. Storto, N. Ferry, M. Valdivieso, K. Haines, M. Balmaseda, H. Zuo, M. Drevillon, and L. Parent, An ensemble of eddy-permitting global ocean reanalyses from the MyOcean project. *Climate Dynamics*, 1–29, 2015.

Mathis, J. T., R. S. Pickart, D. A. Hansell, D. Kadko, and N. R. Bates, Eddy transport of organic carbon and nutrients from the Chukchi Shelf: Impact on the upper halocline of the western Arctic Ocean, *Journal of Geophysical Research, 112*, C05011, doi:10.1029/2006JC003899, 2007.

Mathis, J. T., R. S. Pickart, R. H. Byrne, C. L. McNeil, G. W. K. Moore, L. W. Juranek, X. Liu, J. Ma, R. A. Easley, M. M. Elliot, J. N. Cross, S. C. Reisdorph, F. Bahr, J. Morison, T. Lichendorf, and R. A. Feely, Storm-induced upwelling of high pCO_2 waters onto the continental shelf of the western Arctic Ocean and implications for carbonate mineral saturation states, *Geophysical Research Letters, 39*, L07606, doi:10.1029/2012GL051574, 2012.

McClelland, J. W., R. M. Holmes, K. H. Dunton, and R. W. Macdonald, The Arctic Ocean Estuary, *Estuaries and Coasts, 35*, 353-368, 2012.

McLaughlin, F., E. Carmack, A. Proshutinsky, R. A., Krishfield, C. Guay, M. Yamamoto-Kawai, J. M. Jackson, and B. Williams, The rapid response of the Canada Basin to climate forcing: From bellwether to alarm bells. *Oceanography, 24*, 146-159, 2011.

Mehrbach, C., C. H. Culberson, J. E. Hawley, and R. M. Pytkowicz, Measurement of the apparent dissociation constants of carbonic acid in seawater at atmospheric pressure, *Limnology & Oceanography, 18*, 897-907, doi:10.4319/lo.1973.18.6.0897, 1973.

Melling, H., The formation of a haline shelf front in wintertime in an ice-covered arctic sea, *Continental Shelf Research, 13*, 1123-1147, 1993.

Mucci, A., B. Lansard, L. A. Miller, and T. N. Papakyriakou, CO_2 fluxes across the air-sea interface in the southeastern Beaufort Sea: Ice-free period, *Journal of Geophysical Research, 115*, C04003, doi:10.1029/2009JC005330, 2010.

Nikolopoulos A., R. S. Pickart, P. S. Fratantoni, K. Shimada, D. J. Torres, and E. P. Jones, The western Arctic boundary current at 152ºW: Structure, variability, and transport, *Deep-Sea Research II, 56*, 1164-1181, 2009.

Orr, J. C., V. J. Fabry, O. Aumont, L. Bopp, S. C. Doney, R. A. Feely, A. Gnanadesikan, N. Gruber, A. Ishida, F. Joos, R. M. Key, K. Lindsay, E. Maier-Reimer, R. Matear, P. Monfray, A. Mouchet, R. G. Najjar, G.-K. Plattner, K. B. Rodgers, C. L. Sabine, J. L. Sarmiento, R. Schlitzer, R. D. Slater, I. J. Totterdell, M.-F. Weirig, Y. Yamanaka, and A. Yool, Anthropogenic ocean acidification over the twenty-first century and its impact on calcifying organisms, *Nature, 437*, 681–686, 2005.

Pickart, R. S., Shelfbreak circulation in the Alaskan Beaufort Sea: Mean structure and variability, *Journal of Geophysical Research, 109*, C04024, doi:10.1029/2003JC001912, 2004.

Pickart, R. S., G. W. K. Moore, D. J. Torres, P. S. Fratantoni, R. A. Goldsmith, and J. Yang, Upwelling on the continental slope of the Alaskan Beaufort Sea: Storms, ice, and oceanographic response, *Journal of Geophysical Research, 114*, C00A13, doi:10.1029/2008JC005009, 2009.

Pickart, R. S., M. A. Spall, and J. T. Mathis, Dynamics of upwelling in the Alaskan Beaufort Sea and associated shelf-basin fluxes, *Deep-Sea Research I, 76*, 35-51, 2013.

Proshutinsky, A., D. Dukhovskoy, M.-L. Timmermans, R. Krishfield, and J. L. Bamber, Arctic circulation regimes, *Philosophical Transactions of the Royal Society A, 373*, 20140160, doi:10.1098/rsta.2014.0160, 2015.

Rabe, B., M. Karcher, U. Schauer, J. M. Toole, R. A. Krishfield, S. Pisarev, F. Kauker, R. Gerdes, and T. Kikuchi, An assessment of Arctic Ocean freshwater content changes from the 1990s to the 2006-2008 period, *Deep-Sea Research I, 58*, 173-185, 2011.

Ries, J. B., Skeletal mineralogy in a high-CO_2 world, *Journal of Experimental Marine Biology and Ecology, 403*, 54-64, 2011.

Rudels, B., L. G. Anderson, and E. P. Jones, Formation and evolution of the surface mixed layer and halocline of the Arctic Ocean, *Journal of Geophysical Research, 101*, 8807-821, 1996.

Shadwick, E. H., H. Thomas, M. Chierici, B. Else, A. Fransson, C. Michel, L. A. Miller, A. Mucci, A. Niemi, T. N. Papakyriakou, and J.-É. Tremblay, Seasonal variability of the inorganic carbon system in the Amundsen Gulf region of the southeastern Beaufort Sea, *Limnology & Oceanography, 56*, 303-322, doi:10.4319/lo.2011.56.1.0303, 2011a.

Shadwick, E. H., H. Thomas, Y. Gratton, D. Leong, S. A. Moore, T. Papakyriakou, and A. E. F. Prowe, Export of Pacific carbon through the Arctic Archipelago to the North Atlantic, *Continental Shelf Research, 31*, 806-816, 2011b.

Shadwick, E. H., T. W. Trull, H. Thomas, and J. A. E. Gibson, Vulnerability of polar oceans to anthropogenic acidification: Comparison of Arctic and Antarctic seasonal cycles, *Scientific Reports, 3*, 2339, doi:10.1038/srep02339, 2013.

Shimada, K., T. Kamoshida, M. Itoh, S. Nishino, E. Carmack, F. McLaughlin, S. Zimmermann, and A. Proshutinsky, Pacific Ocean inflow: Influence on catastrophic reduction of sea ice cover in the Arctic Ocean, *Geophysical Research Letters, 33*, L08605, doi:10.1029/2005GL025624, 2006.

Smith, G. C., F. Roy, P. Mann, F. Dupont, B. Brasnett, J.-F. Lemieux, S. Laroche, and S. Bélair, A new atmospheric dataset for forcing ice-ocean models: Evaluation of reforecasts using the Canadian global deterministic prediction system, *Quarterly Journal of the Royal Meteorological Society, 140*, 881-894, 2014.

Stewart, K. D., and T. W. N. Haine, Wind-driven Arctic freshwater anomalies, *Geophysical Research Letters, 40*, 6196-6201, doi:10.1002/2013GL058247, 2013.

Swift, J. H., E. P. Jones, K. Aagaard, E. C. Carmack, M. Hingston, R. W. Macdonald, F. A. McLaughlin, and R. G. Perkin, Waters of the Makarov and Canada basins, *Deep-Sea Research II, 44*, 1503-1529, 1997.

Tremblay, J.-É., P. Raimbault, N. Garcia, B. Lansard, M. Babin, and J. Gagnon, Impact of river discharge, upwelling and vertical mixing on the nutrient loading and productivity of the Canadian Beaufort Shelf, *Biogeosciences, 11*, 4853-4868, 2014.

Williams, J. W., and E. C. Carmack, The 'interior' shelves of the Arctic Ocean: Physical oceanographic setting, climatology and effects of sea-ice retreat on cross-shelf exchange, *Progress in Oceanography, 139*, 24-41, 2015.

Williams, W. J., E. C. Carmack, K. Shimada, H. Melling, K. Aagaard, R. W. Macdonald, and R. G. Ingram, Joint effects of wind and ice motion in forcing upwelling in Mackenzie Trough, Beaufort Sea, *Continental Shelf Research, 26*, 2353-2366, 2006.

Williams, W. J., H. Melling, E. C. Carmack, and R. G. Ingram, Kugmallit Valley as a conduit for cross-shelf exchange on the Mackenzie Shelf in the Beaufort Sea, *Journal of Geophysical Research, 113*, C02007, doi:10.1029/2006JC003591, 2008.

Winde, V., M. E. Böttcher, P. Escher, P. Böning, M. Beck, G. Liebezeit, and B. Schneider, Tidal and spatial variations of $DI^{13}C$ and aquatic chemistry in a temperate tidal basin during winter time, *Journal of Marine Sciences, 129*, 396-404, 2014.

Wood, K. R., J. E. Overland, S. A. Salo, N. A. Bond, W. J. Williams, and X. Dong, Is there a "new normal" climate in the Beaufort Sea? *Polar Research, 32*, 19552, doi:10.3402/polar.v32i0.19552, 2013.

Woodgate, R. A., T. J. Weingartner, and R. Lindsay, Observed increases in Bering Strait oceanic fluxes from the Pacific to the Arctic from 2001 to 2011 and their impacts on the Arctic Ocean water column, *Geophysical Research Letters, 39*, L24603, doi:10.1029/2012GL054092, 2012.

Yamamoto-Kawai, M., F. A. McLaughlin, E. C. Carmack, S. Nishino, K. Shimada, and N. Kurita, Surface freshening of the Canada Basin, 2003-2007: River runoff versus sea ice meltwater, *Journal of Geophysical Research, 114*, C00A05, doi:10.1029/2008JC005000, 2009.

Yamamoto-Kawai, M., F. A. McLaughlin, and E. C. Carmack, Effects of ocean acidification, warming and melting of sea ice on aragonite saturation of the Canada Basin surface water, *Geophysical Research Letters, 38*, L03601, doi:10.1029/2010GL045501, 2011.

Yamamoto-Kawai, M., F. McLaughlin, and E. Carmack, Ocean acidification in the three oceans surrounding northern North America, *Journal of Geophysical Research: Oceans, 118*, 6274-6284, 2013.

Yang, J., The seasonal variability of the Arctic Ocean Ekman transport and its role in the mixed layer heat and salt fluxes, *Journal of Climate, 19*, 5366-5387, 2006.

Yi, Y., J. J. Gibson, L. W. Cooper, J.-F. Hélie, S. J. Birks, J. W. McClelland, R. M. Holmes, and B. J. Peterson, Isotopic signals (^{18}O, ^{2}H, ^{3}H) of six major rivers draining the pan-Arctic watershed, *Global Biogeochemical Cycles, 26*, GB1027, doi:10.1029/2011GB004159, 2012.

Zeebe, R. E., and D. Wolf-Gladrow, *CO_2 in Seawater: Equilibrium, Kinetics, Isotopes*, Elsevier, Amsterdam, 2001.